

# Semi-convection in rotating spherical shells: flows, layers, and dynamos

Paul Pružina<sup>†</sup>, Nathanaël Schaeffer, David Cébron

Université Grenoble Alpes, CNRS, ISTerre, 38000 Grenoble, France

(Received xx; revised xx; accepted xx)

Large regions of gaseous planets are thought to be stratified with an unstable thermal gradient, but a stabilising gradient of heavy element composition. Fluid in these regions is unstable to semi-convection, with motions driven by differences in the molecular diffusivity of temperature and composition, and could play a role in supporting planetary magnetic fields. Previous studies focus largely on local models in Cartesian boxes; here, we investigate semi-convection in rotating spherical shells. The onset of linear instability shows a transition between the two limits of rotating convection and non-rotating semi-convection. Non-linear simulations evolve into a system of concentric layers of relatively constant density, separated by narrow high-gradient regions. These layers gradually merge, resulting in a statistically steady state dominated by either a single convection region or a narrower convective zone beneath a stably stratified layer (SSL), depending on the strength of the thermal forcing compared to the rotation. When magnetic field generation is considered, our magnetohydrodynamic simulations exhibit self-sustained dynamo action. In cases where the turbulent convective region generates magnetic fields that are smoothed by zonal flows within the overlying SSL, the resulting field is strongly dipolar and axisymmetric, in encouraging agreement with Saturn's observed magnetic field. Within the regimes explored, both the Rossby number and the thickness of the SSL are well predicted by a single combination of control parameters. This enables the identification of a parameter range in which the generated magnetic fields resemble those of planetary dynamos.

## 1. Introduction

Fluids that are convectively stable due to a bottom-heavy compositional gradient, but with a destabilising thermal gradient (i.e. stable according to the Ledoux condition, but unstable by the Schwarzschild condition), may undergo an instability known as semi-convection (SC) or oscillatory double-diffusive convection (ODDC). Semi-convection is one regime of double diffusive convection, an instability caused by the effect on the density of two scalars that diffuse at different rates. For example, in gas giant planets, the thermal diffusivity can be up to 100 times the diffusivity of heavy elements (French *et al.* 2012). The opposite regime, in which the thermal gradient is stable, but a compositional gradient is unstable, is referred to as (salt) fingering, (from early studies in oceanic contexts). The transport properties of a semi-convective fluid are significantly different to one that is Schwarzschild stable, with significantly enhanced transport of heat and composition compared to purely diffusive processes (Wood *et al.* 2013).

In astrophysics, semi-convection is of particular interest in gaseous planets such as Jupiter and Saturn (Müller *et al.* 2020; Stevenson *et al.* 2022). These planets are composed of a surface layer of molecular hydrogen, which overlays a deep core of

<sup>†</sup> Email address for correspondence: pruzinap@univ-grenoble-alpes.fr

metallic hydrogen, which has high electrical conductivity. The fluid density is affected by both the temperature and the chemical composition, namely the relative fraction of helium in the metallic hydrogen layer. Recent structure models predict the existence of wide regions with destabilising temperature gradients, but stabilising compositional gradients, resulting in a convectively stable state. Debras & Chabrier (2019) showed that to reproduce observations from Juno and Galileo, the internal structure of Jupiter must contain a stably stratified layer between two convective envelopes, between about 80 and 90% of the planetary radius. A destabilising temperature gradient must exist in this region to match the thermal properties of the interior and external convective zones, providing the necessary conditions for semi-convection. Likewise, Leconte & Chabrier (2012, 2013) suggest that a region of semi-convection could explain Saturn's excessively high luminosity. Mankovich & Fuller (2021) proposed an interior model of Saturn consistent with gravity and seismic data, with a stably stratified region extending to 60% of the planetary radius. Similar semi-convective regions are also predicted at the edge of the convective cores of intermediate and high-mass stars (e.g. Schwarzschild & Härm 1958; Merryfield 1995). Semi-convection also occurs in terrestrial polar oceans (where it is called 'diffusive convection'), with the stabilising compositional gradient provided by salinity (e.g. Timmermans *et al.* 2008).

Semi-convection is sometimes referred to in astrophysical literature as 'layered convection', in reference to the tendency of semi-convective fluids to spontaneously form 'staircases' consisting of well-mixed layers separated by sharp density jumps. This phenomenon is well-documented in periodic box simulations (e.g. Rosenblum *et al.* 2011; Mirouh *et al.* 2012), and more recently in full sphere simulations (Fuentes 2025). Layer formation is due to the so-called  $\gamma$ -instability (Radko 2003), where competing influences of thermal and compositional fluxes lead to a secondary instability on the semi-convective state. Pružina (2025) proposed a one-dimensional model of this layering process for parameters relevant to planetary applications. The effect of rotation on layer formation was studied in 3D periodic boxes by Moll & Garaud (2016), who showed that layer formation can be suppressed at fast rotation rates. Fuentes *et al.* (2024) dispute this, arguing that, in fact, once a staircase has formed, rotation prolongs its lifespan, and that the results of Moll & Garaud (2016) may be due to box-size constraints, with larger domains allowing staircases to form. More recently, Fuentes (2025) presented simulations of full spheres in which faster rotation rates were associated with longer-lasting layered structures, although in all cases the layers gradually coarsen through mergers until a single convective region fills the domain. This gradual coarsening is widely documented across numerical studies of layering (Radko 2003; Mirouh *et al.* 2012; Pružina 2025), following a pattern described by Radko (2007). However, such merging has not yet been convincingly demonstrated in observational studies. So far, the majority of work on astrophysical semi-convection has focused on the layered regime (e.g. Moll & Garaud 2016; Fuentes *et al.* 2024; Fuentes 2025), leaving behaviour outside layered states relatively unexplored.

A particular feature of interest is whether semi-convection can support planetary magnetic fields. Previous work has generally assumed that planetary dynamos are generated by convective motions due to an overall statically unstable density gradient (e.g. Christensen & Aubert 2006; Jones 2014; Yadav *et al.* 2022), but recent work predicting semi-convective regions (e.g. Leconte & Chabrier 2013; Vazan *et al.* 2016; Debras & Chabrier 2019) raises the question of whether semi-convection-driven dynamos are possible. There are few prior studies on this subject, with Mather & Simitev (2021) concluding that while semi-convection dynamos in spherical shells are possible, they require parameter values far from true astrophysical conditions. Pružina *et al.* (2025) demonstrated that simulations of semi-convection can indeed support dynamo action at

low  $Pm$ , showing a simulation where a deep convective dynamo is overlain by a stably stratified layer, producing a rather dipolar magnetic field on the surface. However, this was only a preliminary demonstration, and the detailed behaviour of semi-convection dynamos remains an open question.

While the subject of this work is semi-convection, the related problem of fingering convection in a full sphere was studied by Monville *et al.* (2019). They found that, compared with pure thermal or compositional convection, fingering convection increased the parameter range for linear instability, leading to large-scale convective motions and strong zonal jets. (Gray *et al.* 2025) have recently performed a more detailed study, finding a wide variety of flows including clustering of fingers, toroidal gyres, hemispherical convection, and zonal flows, depending on the relative strengths of the thermal stratification and rotation. It seems likely that a similar range of dynamical structures may be possible in the semi-convection regime.

To model the semi-convective layer of gaseous planets, we investigate semi-convection in a spherical shell, with fixed temperature and compositional boundary conditions to simulate steady convecting layers above and below. We first perform a linear analysis, finding results similar to those of Monville *et al.* (2019), with a linear onset curve that connects the limits of rotating thermal convection and non-rotating semi-convection. Non-linear simulations pass through a transient layered phase, eventually saturating in a state either dominated by strong zonal jets, with a wide stably stratified layer overlaying an inner convective region, or a structure where a single convective zone takes up the entire domain, except for narrow thermal boundary layers. We find that the layering instability conforms well to the predictions of the  $\gamma$ -instability (Radko 2003), but we also confirm the comment of Fuentes *et al.* (2024) that the size of the domain can constrain the development of layers. We investigate the onset of dynamo action and discuss the effect of different flow structures on the magnetic field. We find that a dipolar structure is favoured in the jet-dominated flow regime with a wide SSL, where a magnetic field is generated in the inner convective layer, but decays as a function of radius in the SSL. The dipolar component decays the slowest, resulting in a much more dipolar surface field than in the interior. On this basis, we identify a region of parameter space that is most favourable to producing planetary-like magnetic fields, and compare simulations in this region to Saturn's magnetic field.

The paper is structured as follows. In § 2 we introduce the equations of thermocompositional convection and discuss the non-dimensional parameters governing the flow. In § 3 we review the hydrodynamic stability of the system, with a summary of key stability results for a non-rotating fluid in § 3.1, and calculations of the linear onset of rotating semiconvection in § 3.2, and non-linear simulations in § 4, discussing separately the layered phase of evolution, the saturated states, and the different flow regimes that develop. Finally, in § 5, we present the results of magnetohydrodynamic simulations, and propose a criterion for producing planetary-like magnetic fields in simulations.

## 2. Governing equations of thermocompositional convection

We consider a fluid in a spherical shell of inner radius  $R_i$  and outer radius  $R_o$ , rotating at a rate  $\Omega_0 = \Omega_0 \mathbf{e}_z$ , as shown in figure 1. We adopt spherical polar coordinates, with radial, polar and azimuthal basis vectors  $\{\mathbf{e}_r, \mathbf{e}_\theta, \mathbf{e}_\phi\}$  and position vector  $\mathbf{r}$  such that  $\theta = 0$  for  $\mathbf{r} = \mathbf{e}_z$ . The fluid velocity  $\mathbf{u} = u_r \mathbf{e}_r + u_\theta \mathbf{e}_\theta + u_\phi \mathbf{e}_\phi$  evolves according to the Navier-Stokes equations. We adopt the Boussinesq approximation, which neglects differences in density except in terms multiplied by gravitational acceleration. The magnetic field  $\mathbf{b}$  evolves according to the induction equation, and affects the velocity through the

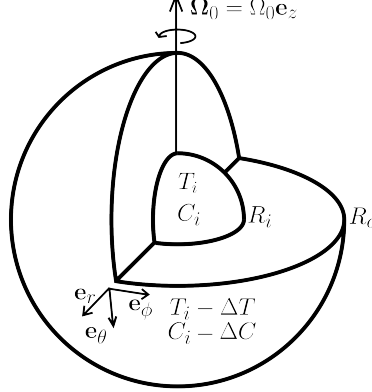


FIGURE 1. Sketch of the physical setup for the problem.

Symbol	Name	Definition	Interpretation
$\rho_0$	Reference density		
$\nu$	Viscous diffusivity		
$\mu_0$	Vacuum magnetic permeability		
$\kappa_T$	Thermal diffusivity		
$\kappa_C$	Compositional diffusivity		
$\eta$	Magnetic diffusivity		
$\alpha_T$	Thermal expansion coefficient		
$\alpha_C$	Compositional contraction coefficient		
$R_o$	Outer radius		
$R_i$	Inner radius		
$E_k$	Ekman number	$\nu / (R_o^2 \Omega)$	Viscous/Coriolis forces
$Pr$	Prandtl number	$\nu / \kappa_T$	Viscous/thermal diffusion
$Sc$	Schmidt number	$\nu / \kappa_C$	Viscous/compositional diffusion
$L$	Lewis number	$Pr/Sc$	Diffusivity ratio
$Pm$	Magnetic Prandtl number	$\nu / \eta$	Viscous/magnetic diffusion
$\Delta R$	Shell thickness	$(R_o - R_i) / R_o$	Aspect ratio
$Ra_T$	Thermal Rayleigh number	$\alpha_T g \Delta T R_o^3 / (\kappa_T \nu)$	Thermal gradient
$Ra_C$	Compositional Rayleigh number	$\alpha_C g \Delta C R_o^3 / (\kappa_C \nu)$	Compositional gradient
$R_\rho$	Density ratio	$ Ra_C  / ( Ra_T  L)$	Compositional/thermal gradient
$Re$	Reynolds number	$UL / \nu$	Inertia/viscous diffusion
$Rm$	Magnetic Reynolds number	$UL / \eta$	Inertia/magnetic diffusion
$R_B$	'Rotational buoyancy number'	$E_k^{3/2} Ra_T Pr^{-1}$	Thermal forcing/rotation

TABLE 1. Dimensional and dimensionless parameters governing the dynamics of rotating semi-convection.

Lorentz force. We adopt a linear equation of state, with the density  $\rho$  depending on temperature  $T$  and composition  $C$ , which obey advection-diffusion equations in the presence of background fields  $T_0$  and  $C_0$ . We assume a constant gravitational acceleration in the radial direction  $\mathbf{g} = -g\mathbf{e}_r$ . In gas giants, this is not an unreasonable assumption: for Saturn, the data of Movshovitz *et al.* (2020) give a difference of only 20% between  $g(0.1R_o)$  and  $g(0.7R_o)$ . We write the thermal and compositional differences across the depth are  $\Delta T = T_0(R_i) - T_0(R_o)$  and  $\Delta C = C_0(R_i) - C_0(R_o)$ , respectively.

The dynamics depend on a number of physical parameters, which are defined in Table 1.

Using these parameters, and with a length-scale based on the sphere's outer radius  $R_o$ , and the timescale of viscous diffusion  $\tau_\nu = R_o^2/\nu$ , we adopt dimensionless variables

$$\mathbf{x} = \frac{\hat{\mathbf{x}}}{R_o}, \quad t = \frac{\nu}{R_o^2} \hat{t}, \quad \mathbf{u} = \frac{R_o}{\nu} \hat{\mathbf{u}}, \quad T = \frac{g\alpha_T R_o^3}{\nu^2} \hat{T}, \quad C = \frac{g\alpha_C R_o^3}{\nu^2} \hat{C}, \quad \mathbf{b} = \frac{R_o}{\nu\sqrt{\rho_0\mu_0}} \hat{\mathbf{b}}, \quad (2.1)$$

where hats denote dimensional quantities. The dynamics are governed by the non-dimensional system of equations

$$\frac{\partial}{\partial t} \mathbf{u} + \left( \frac{2}{\text{Ek}} \mathbf{e}_z + \nabla \times \mathbf{u} \right) \times \mathbf{u} = -\nabla p - (T - C) \mathbf{e}_r + (\nabla \times \mathbf{b}) \times \mathbf{b} + \nabla^2 \mathbf{u} \quad (2.2)$$

$$\frac{\partial}{\partial t} T + (\mathbf{u} \cdot \nabla) (T + T_0) = \frac{1}{\text{Pr}} \nabla^2 T, \quad (2.3)$$

$$\frac{\partial}{\partial t} C + (\mathbf{u} \cdot \nabla) (C + C_0) = \frac{1}{\text{Sc}} \nabla^2 C, \quad (2.4)$$

$$\frac{\partial}{\partial t} \mathbf{b} = \nabla \times (\mathbf{u} \times \mathbf{b} - \frac{1}{\text{Pm}} \nabla \times \mathbf{b}), \quad (2.5)$$

together with the solenoidal constraints  $\nabla \cdot \mathbf{u} = \nabla \cdot \mathbf{b} = 0$ . The dimensionless numbers Ek, Pr, Sc and Pm are defined in Table 1. For the majority of this work, we shall consider only the hydrodynamic problem (i.e. with  $\mathbf{b} \equiv \mathbf{0}$ ); we return to the full magneto-hydrodynamic system in § 5.

A steady basic state exists with  $\mathbf{u} = \mathbf{0}$ , and background temperature and salinity fields given by

$$T_0(r) = \frac{\text{Ra}_T}{\text{Pr}} \delta(r), \quad C_0(r) = \frac{\text{Ra}_C}{\text{Sc}} \delta(r), \quad (2.6)$$

where the thermal and compositional Rayleigh numbers are defined in Table 1, and  $\delta(r)$  is the spherically symmetric solution to Laplace's equation  $\nabla^2 \delta = 0$  in a spherical shell:

$$\delta(r) = \frac{1 - \Delta R}{\Delta R} \frac{1 - r}{r} \quad (2.7)$$

such that  $\delta(1 - \Delta R) = 1$  and  $\delta(1) = 0$ .

To approximate the effect of convective regions above and below the domain, we fix the temperature and composition on the boundaries. The different temperatures and compositions above and below are accounted for by the background fields  $T_0$  and  $C_0$ , so the perturbation fields are set to zero. The velocity obeys a no-flux condition on the boundaries:

$$T = C = \frac{\partial}{\partial r} \left( \frac{u_\theta}{r} \right) = \frac{\partial}{\partial r} \left( \frac{u_\phi}{r} \right) = \mathbf{e}_r \cdot \mathbf{u} = 0 \text{ at } r = 1 - \Delta R, 1 \quad (2.8)$$

### 3. Hydrodynamic stability

In this section, we present a number of linear stability results relevant to semi-convection. First, in § 3.1, we detail the classical stability properties resulting from a local analysis in a non-rotating geometry, before in § 3.2 conducting a detailed linear analysis of perturbations to the basic state (2.6) to find the linear onset of semi-convection in a rotating spherical shell.

#### 3.1. Local stability of non-rotating fluids

Here, we summarise some key results from the local stability analysis of a non-rotating, non-magnetic stratified fluid. The density gradient can be used to define the Brunt-

Väisälä frequency  $N$ , defined as the frequency at which a vertically displaced particle will oscillate in the stratified environment. In dimensional form,  $N^2$  is given by

$$N^2 = -g \mathbf{e}_r \cdot \nabla \left( \frac{\rho}{\rho_0} \right). \quad (3.1)$$

A generalisation can be made to split the background frequency  $N_0^2$  into contributions from temperature and composition such that  $N_0^2 = N_{0,T}^2 + N_{0,C}^2$  as follows

$$N_{0,T}^2 = g \mathbf{e}_r \cdot \nabla T_0, \quad N_{0,C}^2 = -g \mathbf{e}_r \cdot \nabla C_0. \quad (3.2)$$

In dimensionless form, with the background states given by (2.6), these are given by

$$N_{0,T}^2 = -\frac{\text{Ra}_T}{\text{Pr}} \frac{1 - \Delta R}{\Delta R} \frac{1}{r^2}, \quad N_{0,C}^2 = +\frac{\text{Ra}_C}{\text{Sc}} \frac{1 - \Delta R}{\Delta R} \frac{1}{r^2} \quad (3.3)$$

The Schwarzschild criterion (Schwarzschild 1958) states that a fluid is stable to thermal convection if

$$N_{0,T}^2 > 0. \quad (3.4)$$

The related Ledoux criterion (Ledoux 1947), which includes the effects of composition, states that a fluid is stable to convective motions if

$$N_0^2 > 0. \quad (3.5)$$

Semi-convection refers to the regime where the fluid is Ledoux-stable, but Schwarzschild unstable, i.e.

$$N_0^2 > 0 \quad \text{and} \quad N_{0,T}^2 < 0, \quad (3.6)$$

or, in terms of the Rayleigh numbers,

$$\text{Ra}_T, \text{Ra}_C > 0. \quad (3.7)$$

Despite being stable to convection according to the Ledoux criterion (3.5), double diffusive instabilities can occur (in a non-rotating fluid) if

$$\frac{\text{Ra}_T}{\text{Pr}} > \frac{\text{Pr} + 1/L}{\text{Pr} + 1} \frac{\text{Ra}_C}{\text{Sc}} + \left(1 + \frac{1}{L}\right) \left(1 + \frac{1}{L\text{Pr}}\right) \frac{27\pi^4}{4}, \quad (3.8)$$

where  $L = \kappa_T/\kappa_C = \text{Sc}/\text{Pr}$  is the Lewis number or diffusivity ratio (e.g. Turner 1979). For sufficiently high Rayleigh numbers, the second term may be neglected. The range of double-diffusive instability is commonly discussed in terms of the density ratio

$$R_\rho = \frac{\alpha_C |\nabla C_0|}{\alpha_T |\nabla T_0|} = \frac{1}{L} \frac{|\text{Ra}_C|}{|\text{Ra}_T|}. \quad (3.9)$$

$R_\rho$  is defined by (3.9) for semi-convection, but by its inverse in the fingering regime, such that  $R_\rho$  is always greater than unity in the double-diffusive regime of interest.

Rewriting (3.8) in terms of  $R_\rho$ , semi-convection occurs in the range

$$1 \leq R_\rho \leq \frac{\text{Pr} + 1}{\text{Pr} + 1/L}, \quad (3.10)$$

with the fluid statically stable for larger values of  $R_\rho$ , and convectively unstable by (3.5) for smaller values. Note that if  $\text{Pr}$  is large, then the range of  $R_\rho$  for semi-convection becomes very narrow; this is effectively the limit of no diffusion. In astrophysical fluids,  $\text{Pr}$  is generally much less than unity, so semi-convection can occur across a wide range of density ratios.

The formation of staircases is due to a secondary instability which acts on the fields

resulting from the double-diffusive instability. The  $\gamma$ -instability theory (Radko 2003) states that if  $F_T$  and  $F_C$  are the turbulent temperature and compositional fluxes, and  $\gamma = F_C/F_T$  is their ratio, then layers will form if

$$\frac{\partial \gamma}{\partial R_\rho} < 0. \quad (3.11)$$

Similarly to  $R_\rho$ ,  $\gamma$  is generally defined as its reciprocal in the fingering regime, so condition (3.11) is unchanged.

In practice, (3.11) is satisfied in a range

$$1 \leq R_\rho \leq R_{\max}^* < \frac{\text{Pr} + 1}{\text{Pr} + 1/L}, \quad (3.12)$$

where the specific value of  $R_{\max}$  depends on the specific parameters of the fluid (e.g. Pružina 2025). However, condition (3.11) requires  $\partial\gamma/\partial R_\rho$  to be calculated across a range of simulations for different values of  $R_\rho$ ; there is still no predictive condition for layer formation based on the input parameters of a single simulation.

### 3.2. Linear onset of rotating semi-convection in a spherical shell

In this section, we report on the linear onset of instability, determining the shape of the unstable regions in Rayleigh number space and the dependence on the Ekman number. We take  $\text{Pr} = 0.3$  and  $\text{Sc} = 3$ , giving a Lewis number of 10. These values are commonly used for simulations of astrophysical fluids, as they allow the low-Pr regime to be captured, while remaining numerically accessible at relatively low resolutions (e.g. Breuer *et al.* 2010). For the linear calculations, we take  $\Delta R = 0.5$  as an intermediate size for the shell, noting that a thinner shell would be more computationally demanding. For a number of values of  $\text{Ek}$ , we survey a wide range of values of  $\text{Ra}_C$ , finding the onset of instability.

We use the SINGE linear eigensolver (Vidal & Schaeffer 2015; Monville *et al.* 2019) to find the onset of instability. At each value of  $\text{Ra}_C$ , and each spherical harmonic order  $m$  and equatorial symmetry  $s = \pm 1$ , SINGE finds the critical value  $\text{Ra}_T = \text{Ra}_{T,\text{crit}}$  at which the maximum linear growth rate of eigenmodes is  $\sigma = 0$ . We define the critical Rayleigh number as

$$\text{Ra}_{T,\text{crit}}(\text{Ra}_C) = \min_{m,s}\{\text{Ra}_{T,\text{crit}}^{m,s}(\text{Ra}_C)\} \quad (3.13)$$

For a thermal convection in a rotating spherical shell, Dormy *et al.* (2004) found that the onset of instability followed the scaling  $\text{Ra}_{T,\text{crit}} \sim \mathcal{R}_0 \text{Ek}^{-4/3} + \mathcal{R}_1 \text{Ek}^{-1}$  for a relatively thin shell ( $\Delta R = 0.35$ ). We begin by confirming that this extends to our wider shell by using SINGE to find the critical value  $\text{Ra}_{T,\text{crit}}$  at  $\text{Ra}_C = 0$  for three values of  $\text{Ek}$ . These values are reported in Table 2, and fit the prediction of Dormy *et al.* (2004) perfectly.

Figure 2 shows the onset of instability in Rayleigh-number space, for three values of  $\text{Ek}$ , and  $1 \leq m \leq 40$ . For small values of  $\text{Ra}_T$ , the system is stable; as  $\text{Ra}_T$  increases, the critical threshold  $\text{Ra}_{T,\text{crit}}(\text{Ra}_C)$  is passed and the system becomes unstable. For each value of  $\text{Ek}$ , there are two limiting regimes. Firstly, for small values of  $\text{Ra}_C$ , the system approaches the limit of rotating convection, with

$$\text{Ra}_{T,\text{crit}} \sim \text{Ra}_{T,\text{crit}}(\text{Ra}_C = 0) \quad (3.14)$$

In the opposite limit, for large values of  $\text{Ra}_C$ , the onset of non-rotating semi-convection is approached, with

$$\text{Ra}_{T,\text{crit}} \sim \frac{\text{Ra}_C}{L} \frac{\text{Pr} + 1/L}{\text{Pr} + 1} \quad (3.15)$$

$Ek$	$Ra_{T,\text{crit}}$	$m_{\text{crit}}$	$\omega_{\text{crit}}$
$10^{-4}$	$3.45 \times 10^5$	8	$-5.93 \times 10^2$
$10^{-5}$	$4.24 \times 10^6$	16	$-2.84 \times 10^3$
$10^{-6}$	$5.74 \times 10^7$	28	$-1.89 \times 10^4$

TABLE 2. Critical Rayleigh number and spherical harmonic order at the onset of rotating thermal convection (i.e.  $Ra_C = 0$ ) for three values of  $Ek$ . These values follow the scaling  $Ra_{T,\text{crit}} \sim 0.28Ek^{-4/3} + 30Ek^{-1}$  with an  $R^2$  value of 0.9999, perfectly matching the theory of Dormy *et al.* (2004).

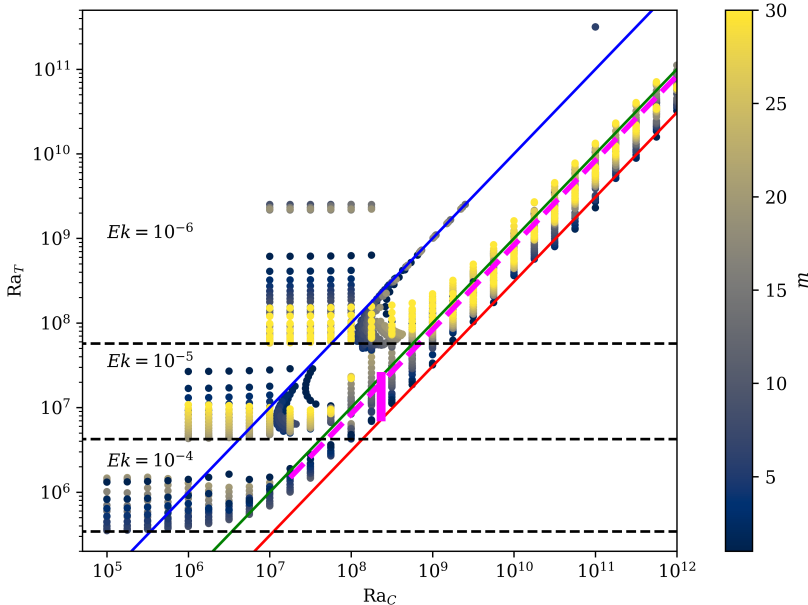


FIGURE 2. Linear onset of semi-convection computed with SINGE, for  $\Delta R = 0.5$ ,  $Pr = 0.3$ ,  $Sc = 3$ , with three values of  $Ek$  and spherical harmonic order  $1 \leq m \leq 40$ . Diagonal lines show (blue)  $Ra_T = Ra_C$ , (green)  $Ra_T = Ra_C/L$ , and (red) the limit of non-rotating semi-convection given by (3.15). The pink lines show the position of transects for non-linear simulations, one with  $R_\rho = 1.2$  while  $Ra_C$  and  $Ra_T$  vary, the other for  $Ra_C = 2.33 \times 10^8$ , and  $1 < R_\rho < 3$ . Horizontal lines show the onset of thermal rotating convection, with values given in Table 2.

In between these two limits, the behaviour depends strongly on the spherical harmonic order  $m$ . For large values of  $m$ , there is a smooth transition between (3.14) and (3.15). For each of the values of  $Ek$  investigated here, this includes the value of  $m$  at the onset for small  $|Ra_C|$ . For smaller  $m$ , the onset curve forms a ‘tongue’ for  $Ra_C/L \leq Ra_T \leq Ra_C$ , extending the unstable range below the small  $Ra_C$  limit for that value of  $m$ . For  $Ek = 10^{-4}$  and  $10^{-5}$ , this tongue does not affect the overall region of instability. However, for  $Ek = 10^{-6}$ , at the smallest values of  $m$ , the tongue reaches values of  $Ra_C$  beneath the rotating convection limit, slightly extending the unstable region.

The existence of the semi-convective tongue mirrors the behaviour reported by Monville *et al.* (2019) for the fingering regime, where the tongue exists for  $Ra_T < Ra_C < LRa_T$ . They found that the tongue extended the range of instabilities for all values of  $Ek$  tested, rather than only the smaller ones. When the data in fig. 2 is plotted in terms of  $EkRa_C$  and  $EkRa_T$  (not shown), the position of the tongue appears to be invariant (for  $m$  such

that it exists), with the same profile for all values of  $\text{Ek}$ . Since viscosity disappears from all the parameters describing the shape of the tongue, Monville *et al.* (2019) described this as an inviscid regime. For semi-convection, however, the position of the lower boundary depends on  $\text{Pr}$ , and hence it cannot truly be described as inviscid.

#### 4. Dynamics in the non-linear regime

We now investigate the dynamics beyond the onset of instability, using the XSHELLS code (Schaeffer 2013; Monville *et al.* 2019) to solve the hydrodynamic Boussinesq equations (2.2)–(2.4) (with  $\mathbf{b} = \mathbf{0}$ ) in a spherical shell of depth  $\Delta R = 0.5$  with boundary conditions (2.8). We first show the results of a single long simulation in fig. 3, for  $\text{Ek} = 10^{-4}$ ,  $\text{Pr} = 0.3$ ,  $\text{Sc} = 3$ , and  $R_\rho = 1.2$ . The system is initialised with a small amplitude random perturbation to the background fields (2.6). Figure 3(a) shows the total kinetic energy as a function of time, showing a linear growth phase, before the energy saturates. It was shown by Monville *et al.* (2019) (and we have verified) that the growth rates obtained in XSHELLS match those predicted by SINGE. After this, the energy settles into quasi-periodic oscillations of amplitude  $\sim 2 \times 10^4$  around a mean of  $E_u \approx 4.5 \times 10^4$ , with statistically stable convective motions continuing for a long time. Figure 3(b)–(f) show equatorial snapshots of the perturbation and total density fields, and meridional snapshots of the radial and azimuthal components of the velocity, at two times after saturation. There is little significant difference between the two snapshots, demonstrating the steady nature of the dynamics once the linear instability has saturated. At both times, the velocity structure takes the form of an inner retrograde and outer prograde zonal jet, with the radial velocity notably slower than the zonal flow. The density field shows a relatively uniform radial gradient, although with large convective structures throughout.

For a stronger density gradient, the evolution is somewhat different. Figure 4a shows the time-evolution of the energy for a simulation with  $\text{Ek} = 10^{-4}$ ,  $\text{Pr} = 0.3$ ,  $\text{Sc} = 3$ ,  $\text{Ra}_T = 1.33 \times 10^9$  and  $R_\rho = 1.2$ . By contrast to fig. 3, after the initial linear growth phase, the energy appears to level off (at  $E_u \approx 1 \times 10^6$ ), before increasing again and saturating at  $E_u \approx 1 \times 10^7$ . Figure 4(b)–(e) show the density and velocity fields during this inflection period: a two-layer density structure is visible, with the density perturbation  $\rho$  decreasing with radius, then increasing sharply before decreasing again. The velocity field shows small-scale convective motions of similar amplitude in both radial and meridional directions. Once the energy saturates, the density layers disappear, forming a single convective region through the entire domain as seen in fig. 4(f), with notably larger velocities than in the first snapshot. The velocity field forms a pair of strong zonal jets, similar to in fig. 3(c), but with the retrograde jet near the equator, and prograde motion nearer the poles. In the rest of this section, we will begin by investigating the early layered phase of the evolution, before addressing the long-term behaviour of the saturated fields.

To characterise the flows observed in our simulations, we define a number of dimensionless parameters. The Reynolds number

$$\text{Re} = \frac{UL}{\nu} = \frac{\sqrt{2\langle E_u \rangle_{\text{rms}}} R_o}{\nu}, \quad (4.1)$$

quantifies the ratio of inertial to viscous effects in the flow. Here,  $L = R_o$  is the characteristic length scale, and  $U = \sqrt{2\langle E_u \rangle_{\text{rms}}}$  is a characteristic velocity based on the root-mean-square kinetic energy density  $\langle E_u \rangle_{\text{rms}} = \int_V \mathbf{u} \cdot \mathbf{u} \, d\mathbf{x} / 2V$ . Turbulent transport of heat and composition throughout the domain is quantified by the Nusselt and Sherwood numbers, defined as the ratio of the total radial scalar transport to purely

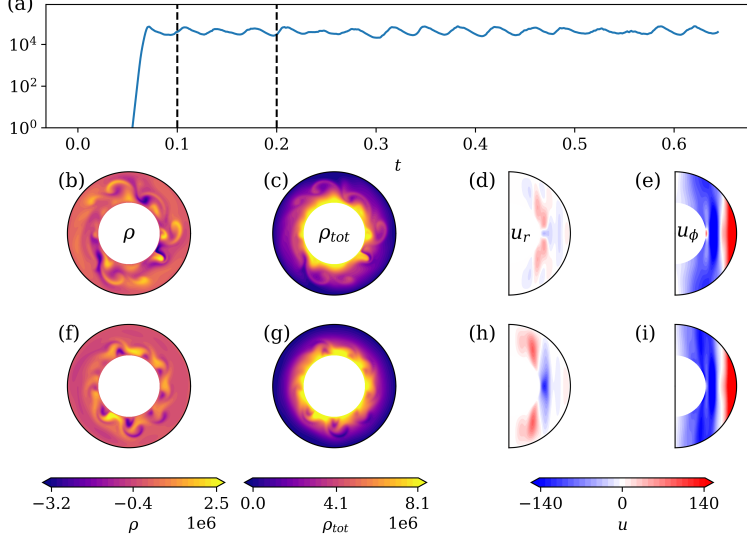


FIGURE 3. Results from an XSHELLS simulation with  $\text{Ek} = 10^{-4}$ ,  $\text{Pr} = 0.3$ ,  $\text{Sc} = 3$ ,  $\Delta R = 0.5$ ,  $\text{Ra}_C = 4.22 \times 10^7$  and  $R_\rho = 1.2$ . (a) Time series of the total kinetic energy  $E_u$ . Second and third row show snapshots of the flow at (b)–(e):  $t = 0.1$  and (f)–(i)  $0.2t_v$ , marked with vertical dashed lines in (a). (b),(f) Equatorial snapshots of the density perturbation  $\rho = C - T$ ; (c),(g) Equatorial snapshots of the total density  $\rho_0 = C_0 + C - T_0 - T$ ; (d),(h) meridional snapshots of the radial velocity  $u_r$ , (e),(i) meridional snapshots of the azimuthal velocity  $u_\phi$ .

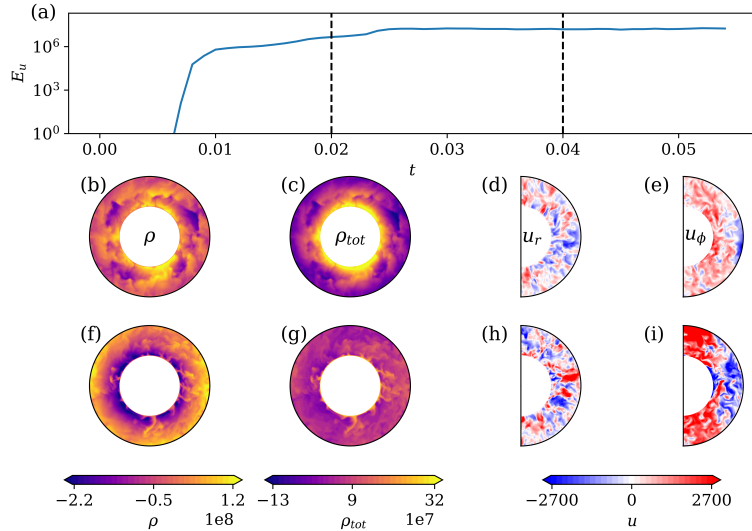


FIGURE 4. Results from an XSHELLS simulation with  $\text{Ek} = 10^{-4}$ ,  $\text{Pr} = 0.3$ ,  $\text{Sc} = 3$ ,  $\Delta R = 0.5$ ,  $\text{Ra}_C = 1.33 \times 10^9$  and  $R_\rho = 1.2$ . (a) Time series of the total kinetic energy  $E_u$ . The second and third row show snapshots of the flow at (b)–(e):  $t = 0.02$  and (f)–(i)  $0.04t_v$ , marked with vertical dashed lines in (a). (b),(f) Equatorial snapshots of the density perturbation  $\rho = C - T$ ; (c),(g) Equatorial snapshots of the total density  $\rho_{tot} = C_0 + C - T_0 - T$ ; (d),(h) meridional snapshots of the radial velocity  $u_r$ , (e),(i) meridional snapshots of the azimuthal velocity  $u_\phi$ .

conductive transport. In general, these are defined at each radius as

$$\text{Nu}(r) = \frac{-\langle u_r (T + T_0) \rangle_S + \text{Pr}^{-1} \langle \partial(T + T_0) / \partial r \rangle_S}{\text{Pr}^{-1} \langle \partial T_0 / \partial r \rangle_S}, \quad (4.2)$$

$$\text{Sh}(r) = \frac{-\langle u_r (C + C_0) \rangle_S + \text{Sc}^{-1} \langle \partial(C + C_0) / \partial r \rangle_S}{\text{Sc}^{-1} \langle \partial C_0 / \partial r \rangle_S}, \quad (4.3)$$

where  $\langle \cdot \rangle_S$  represents the mean across a surface of constant radius. In a purely conductive state,  $\text{Nu} = \text{Sh} = 1$ , the values increase as the intensity of the convection increases. In practice, we evaluate  $\text{Nu}$  and  $\text{Sc}$  at the inner or outer boundary, where the convective fluxes vanish due to the no-penetration condition on the radial velocity:

$$\text{Nu} = \left[ \frac{\langle \partial(T + T_0) / \partial r \rangle_S}{\langle \partial T_0 / \partial r \rangle_S} \right]_{r=0,1}, \quad \text{Sh} = \left[ \frac{\langle \partial(C + C_0) / \partial r \rangle_S}{\langle \partial C_0 / \partial r \rangle_S} \right]_{r=0,1}. \quad (4.4)$$

Also of interest is the convective power, defined as the work done by buoyancy forces, with thermal and compositional components given in dimensionless form by

$$P_T = \langle (T + T_0) u_r \rangle_V, \quad P_C = -\langle (C + C_0) u_r \rangle_V, \quad (4.5)$$

with  $\langle \cdot \rangle_V$  denoting the volume average over the whole domain. In the semi-convection regime, motions are driven by a positive  $P_T$ , while  $P_C$  is negative, opposing fluid motions. Where convection occurs,  $P = P_T + P_C$  is positive.

In general,  $\text{Re}$ ,  $\text{Nu}$ ,  $\text{Sh}$ ,  $P_T$  and  $P_C$  are time-varying quantities, but it is commonly more useful to consider their time average, denoted by an overbar. We define

$$\bar{q} = \frac{1}{t_2 - t_1} \int_{t_1}^{t_2} q(t) dt, \quad (4.6)$$

where  $t_1$  is generally the time at which the kinetic energy saturates, and  $t_2$  is the end of the simulation.

#### 4.1. The layered phase of evolution

In this section, we study the transient layered phase in more detail, quantifying the dependence of the layers on the system parameters and considering their long-term fate. Although double-diffusive layers are well-documented in periodic boxes (e.g. Rosenblum *et al.* 2011; Mirouh *et al.* 2012; Wood *et al.* 2013), significantly less work has been done in a spherical geometry. Recently, Fuentes (2025) conducted simulations of semi-convection in full spheres, finding that the semi-convection instability developed into a series of convective layers, which were gradually eroded by a strong outer layer growing into the interior. In these simulations, faster rotation rates resulted in longer-lasting layers, with the outer convective layer growing towards the centre more slowly. This contradicts Moll & Garaud (2016), who concluded that rotation suppresses the layer formation. Fuentes (2025) argues that in the periodic-box simulations of Moll & Garaud (2016), a relatively small domain suppressed the layering, as the layer height grows with the rotation rate, eventually becoming larger than the domain depth. (We shall discuss the dependence of layer height on forcing and rotation rate in § 4.1.2 Fuentes (2025) avoided this problem with a larger full sphere domain, although the reduced domain depth of  $\Delta R = 0.5$  may have a greater effect in our shell simulations, constraining layer formation to slower-rotating cases.

According to the widely accepted theory of Radko (2003), the layering instability depends only on the density ratio  $R_\rho$ , and a semi-convective fluid will develop density layers if the ratio of the composition to temperature fluxes  $\gamma = F_C/F_T$  decreases as a

function of the density ratio. This theory has been confirmed by numerous works on simulations in both fingering and semi-convection regimes (e.g. Radko 2003; Wood *et al.* 2013). However, this is a linear theory, based on local uniform gradient background states, without the influence of boundaries. The simulations in figures 3–4 use the same value of  $R_\rho$ , but do not both produce layers, showing that in the bounded geometry that we consider, layering must also depend on the stratification. To study the effects of both parameters, we discuss simulations along two transects (marked in fig. 2): with  $\text{Ra}_C$  fixed while  $R_\rho$  varies, and vice versa. In both transects, the strength of the forcing ( $\text{Ra}_T$ ) varies; however, the fixed- $R_\rho$  transect runs approximately parallel to the onset of semi-convection, while the fixed- $\text{Ra}_C$  transect spans the width from semi-convection onset to convection onset.

#### 4.1.1. Effect of $R_\rho$ on layer formation

To measure the effect of  $R_\rho$  on layering, we show simulations with  $\text{Ra}_C = 2.33 \times 10^8$  fixed, and  $1 \leq R_\rho \leq 3$ , for  $\text{Pr} = 0.3$   $\text{Sc} = 3$ ,  $\Delta R = 0.5$ ,  $\text{Ek} = 10^{-4}$ . From the temperature and composition equations (2.3)–(2.4), and the definitions of the background fields (2.6), we define the local radial temperature and composition fluxes as

$$F_T^{local} = \frac{\partial}{\partial r} \left( -\frac{\text{Ra}_T}{\text{Pr}^2} \delta(r) + T \right) - (T + T_0) u_r, \quad (4.7)$$

$$F_C^{local} = \frac{\partial}{\partial r} \left( -\frac{\text{Ra}_C}{\text{Sc}^2} \delta(r) + C \right) - (C + C_0) u_r. \quad (4.8)$$

Taking the volume average across the entire domain, we obtain the mean fluxes in terms of the convective powers,

$$F_T = -\frac{\text{Ra}_T}{\text{Pr}^2} - P_T, \quad F_C = -\frac{\text{Ra}_C}{\text{Sc}^2} + P_C, \quad (4.9)$$

as the volume-mean of the perturbations  $T$  and  $C$  vanish. This gives the flux ratio

$$\gamma = \frac{F_C}{F_T} = \frac{\text{Ra}_C/\text{Sc}^2 - P_C}{\text{Ra}_T/\text{Pr}^2 + P_T}. \quad (4.10)$$

In a pure conductive state (i.e.  $\mathbf{u} = \mathbf{0}$ ), the convective powers are zero, and hence  $\gamma = R_\rho/L$ .

As layering is a secondary instability that acts on the initial semi-convection response,  $\gamma$  must be calculated during the linear phase of a simulation; measuring the fluxes in the saturated post-layering state results in spurious trends in  $\gamma(R_\rho)$  due to the different evolution of the layered compared to non-layered simulations. Figure 5(a) shows how  $\bar{\gamma}$  varies as a function of  $R_\rho$  across a transect of simulations. (While we show a time-average of  $\gamma$ , in principle this is not necessary because the temperature and composition perturbations grow linearly at the same rate.) As  $R_\rho$  increases from 1,  $\bar{\gamma}$  decreases, reaching a minimum at  $R_\rho \approx 1.7$ . Past this critical point,  $\gamma$  increases almost linearly with  $R_\rho$ , becoming very close to the conductive limit  $\bar{\gamma} \sim R_\rho/L$ . This curve closely resembles that found in periodic box simulations by Mirouh *et al.* (2012), and predicts layer formation for  $R_\rho < R_{\rho,\text{layer}} \approx 1.7$ . The colour of the points denotes the value of  $\bar{\text{Re}}$ , showing that as  $R_\rho$  increases, the flow becomes weaker, and a significant drop-off in  $\bar{\text{Re}}$  occurs past the limit of layering. Note that the two simulations with the largest values of  $R_\rho$  are past the onset of rotating semi-convection  $R_{\rho,\text{onset}}$  (i.e. are stable to both convection and semi-convection). In these simulations, mass transfer occurs only via conduction, so they lie exactly on the conductive limit.

Figs 5(b)–(c) show snapshots of the axisymmetric part of the composition field  $C_{axi}$  for

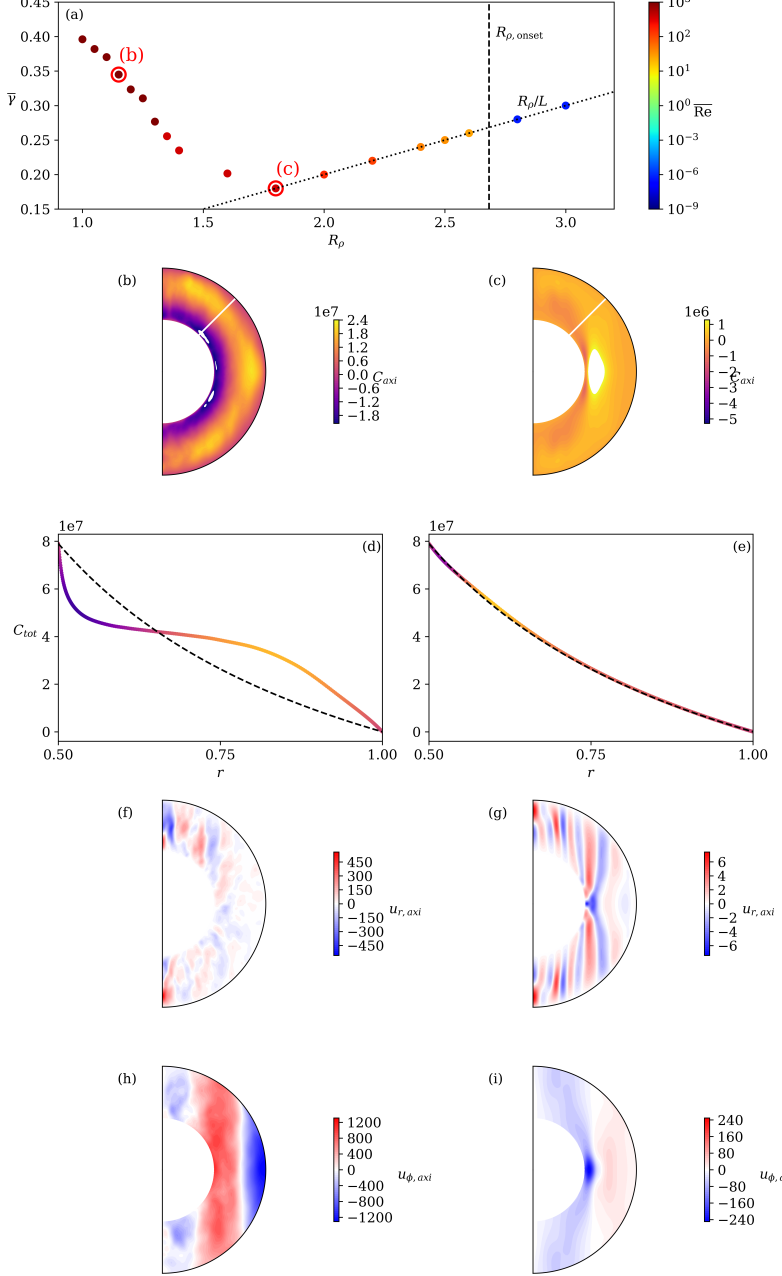


FIGURE 5. (a) Flux ratio time-averaged over the linear phase of evolution  $\bar{\gamma}$  as a function of  $R_\rho$  for simulations along the transect  $\text{Ra}_C = 2.33 \times 10^8$ ,  $1 \leq R_\rho \leq 3$ , with  $\text{Pr} = 0.3$ ,  $\text{Sc} = 3$ ,  $\Delta R = 0.5$ ,  $\text{Ek} = 10^{-4}$ . The values for  $\bar{\gamma}$  are calculated (by (4.10)) during the linear growth phase of each simulation. The vertical dashed line marks the limit of rotating semi-convection  $R_{\rho,\text{onset}} = 2.68$ , calculated using SINGE. Points are coloured by the value of  $\text{Re}$ ; to the right of the semi-convection limit. The dotted black line shows the limit of pure conduction  $R_\rho/L$ . (b),(c) Snapshots of the axisymmetric ( $m = 0$ ) component of the composition field  $C$ , for (b)  $R_\rho = 1.2$  and (c)  $R_\rho = 1.8$ , labelled in red in (a). (d)–(e) radial profiles of the total axisymmetric composition field  $C_{\text{tot}} = C_{\text{axi}} + C_0(r)$  along the white lines in (b)–(d), coloured by the value of  $C_{\text{axi}}$ . Dashed black lines show the conductive profile  $C_0(r)$ .

two simulations (one either side of  $R_{\rho, \text{layer}}$ ), with radial profiles of the total composition field  $C_{\text{tot}} = C_0(r) + C_{\text{axi}}$  shown in fig. 5(d)–(e). We show the composition, rather than total density, as the small Prandtl number (i.e. fast thermal diffusion) means that the temperature profile is rather smeared, making it more difficult to see structures in  $\rho$  than in  $C$ . Where  $R_{\rho} < R_{\rho, \text{layer}} \approx 1.7$  (fig. 5(b), (d)), there is a clear layered structure, with a wide well-mixed region extending across  $0.55 \lesssim r \lesssim 0.75$ . In fig. 5(c), (e), by contrast, no layers are visible, and the total composition field shows little variation from the background conductive profile  $C_0(r)$ . Instead, the semi-convection instability results in a small-amplitude linear response that does not develop into layers. The weak velocities seen in fig. 5(g), (i) result in very small convective fluxes, so the flux ratio is very close to the conductive limit  $\bar{\gamma} \sim R_{\rho}/L$ . As such, there is good agreement with the  $\gamma$ -instability theory, with layers forming where  $\partial\bar{\gamma}/\partial R_{\rho} < 0$ .

Note that the small departure from the conductive profile in fig. 5(e) does not mean that semi-convection is not occurring; according to (3.15), the semi-convection limit is  $R_{\rho, \text{onset}} = 2.67$ . For values in the range  $R_{\rho, \text{layer}} \lesssim R_{\rho} < R_{\rho, \text{onset}}$ , layers do not develop, and instead the long-time state of the field is a small-amplitude weakly nonlinear response, with a Reynolds number (and velocities) two orders of magnitude smaller than in the layered simulation.

#### 4.1.2. Effect of $\text{Ra}_C$ on layer formation

As discussed previously, layering in our simulations depends not only on  $R_{\rho}$ , but on  $\text{Ra}_C$  as well, as demonstrated by figs. 3–4. Fuentes *et al.* (2024) suggest that this may be due to geometric constraints, with the instability scale becoming too large with respect to the domain depth. To investigate the dependence on the stratification, we consider simulations with fixed  $R_{\rho} = 1.2$ , and vary  $\text{Ra}_C$  and  $\text{Ra}_T$ . Thus, the magnitude of the stratification and forcing varies, but the distance from the onset is relatively constant.

Figure 6 shows how the number of layers  $N_l$  depends on  $\text{Ra}_C$  along transects with  $R_{\rho} = 1.2$ , along side snapshots of simulations with zero, one, two and three layers. By rescaling  $\text{Ra}_C \rightarrow \text{EkRa}_C$ , the data from the two transects ( $\text{Ek} = 10^{-4}, 10^{-5}$ ) collapses onto a single trend  $N_l \sim (\text{EkRa}_C)^{1/2}$ . Mixed layers are identified as broad regions where the total composition gradient is notably lower than in the conductive profile  $C_0(r)$ ; where more than one layer exists, they are separated by relatively narrow, high gradient ‘interfaces’.

In our simulations,  $\text{Ra}_T$  and  $\text{Ra}_C$  are varied by changing the background thermal and compositional fields, while keeping the domain depth constant. However, the same change in Rayleigh number could equally be achieved by varying the depth of the domain. In § 2, we defined  $\text{Ra}_C$  in Table 1 using the composition difference across the domain  $\Delta C$ , ‘hiding’ a factor of  $R_o$ . An equivalent definition in terms of the composition gradient,  $\text{Ra}_C = (\alpha_C g R_o^4 \langle \partial C / \partial r \rangle_r) / (\kappa_C \nu)$ , where  $\langle \partial C / \partial r \rangle_r$  is the mean compositional gradient across the domain, makes clear that  $\text{Ra}_C \sim R_o^4$ , and hence  $\text{EkRa}_C \sim R_o^2$ . Hence the transformation  $\Delta C \rightarrow \lambda \Delta C$  has the same effect on  $\text{EkRa}_C$  as  $R_o \rightarrow \lambda^{1/2} R_o = R_{\text{eff}}$ . Assuming that the thickness of a layer  $h_l$  is independent of the domain size, the number of layers that fit in the domain follows  $N_l = R_{\text{eff}}/h_l$ , and hence

$$N_l \sim (\text{EkRa}_C)^{1/2}. \quad (4.11)$$

The black line in fig. 6(a) shows the scaling (4.11); where  $N_l > 0$ , there is broad agreement between the data and 1/2 power law. (Grey lines show upper and lower bounds on the power law at 0.2 and 0.65). Only an integer number of layers is possible, so the scaling (4.11) cannot fit exactly. In particular, when  $\text{Ra}_C$  is below a certain threshold, the domain

is no longer large enough to support layering, and  $N_l = 0$ , matching with the results of Moll & Garaud (2016).

Note the difference between the zero-layer state in fig. 6(b) and that seen in fig. 5(c). Here, layering is possible by the  $\gamma$ -instability, so there is a full non-linear response with convective motions visible in the velocity field, and noticeable density structure visible, but no coherent layering throughout the domain. By contrast, in fig. 5(c), the system is stable to layering, with only a small-amplitude weakly non-linear response. The composition field is rather homogeneous, with no discernible departure from the background conductive state in fig. 5(e).

#### 4.2. Long-term evolution of staircases

It is well-documented that in simulations, density staircases gradually erode through layer merger events, until only a single mixed layer remains in the domain (e.g. Wood *et al.* 2013; Fuentes *et al.* 2024; Pružina 2025). In fig. 6(f)–(i), the solid black lines represent the final profile of  $C_{tot}$  after layers have decayed, showing that in our simulations, there are two possible final states: low values of  $\text{Ra}_C$  lead to a structure comprised of an inner convective region overlain by a wide stably stratified layer, while higher values of  $\text{Ra}_C$  produce a single well-mixed region filling the domain, with narrow boundary layers on either side.

Figure 7 shows the long-term evolution of the radial composition profile for two simulations: one leading to each final state. In fig. 7(a), for the (low- $\text{Ra}_C$ ) simulation labelled (c) in fig. 6(a)), the initially smooth background profile gradually undergoes sharpening, leading to a ‘one-layer’ state, with a single well-mixed layer in the interior, overlain by a stably stratified region. Over time, the mixed layer increases in size, but eventually stabilises far from the outer boundary. This state is remarkably stable for long times. By contrast, in fig. 7(b), (for simulation (e) in fig 6(a)), the initial profile develops into a stack of three mixed layers separated by sharper interfaces, which merge until a single mixed layer takes up the vast majority of the domain, in between narrow stably stratified boundary layers.

For higher values of  $\text{Ra}_C$ , the behaviour of the layers is similar to that seen in other studies, with a gradual erosion of the layered state leading ultimately to a well-mixed state throughout the domain (e.g. Fuentes 2025). However, the final state seen for lower values of  $\text{Ra}_C$  is rather different. This suggests a competition between rotational and convective processes, where the tendency of a rotating fluid to form columnar structures prevents the erosion of the stably stratified outer layer. For these low- $\text{Ra}_C$  simulations, the layered phase never truly ends — in our simulations, the wide convective layer overlain by an SSL survives without further evolution of its size — meaning it can impact the dynamics on long time scales.

Figure 7(c) shows the survival time of the layered state, for simulations resulting in a convective zone throughout the entire domain (it is difficult to define an end of the layered phase when the final state contains a wide SSL). Larger values of  $\text{EkRa}_C$  result in a shorter layered phase, with an approximate scaling  $t_{\text{layer}} \sim (\text{EkRa}_C)^{-1}$ . This agrees with the results of Fuentes *et al.* (2024), who found that higher rotation rates relative to the stratification produced longer-lasting layers, as rotational effects resisted the convection processes, causing layers to merge.

To quantify the transition between the two regimes, we define the boundaries of the convective zone as

$$R_1 = \min\{r | \partial b / \partial r < 0\}, \quad (4.12)$$

$$R_2 = \max\{r | \partial b / \partial r < 0\}. \quad (4.13)$$

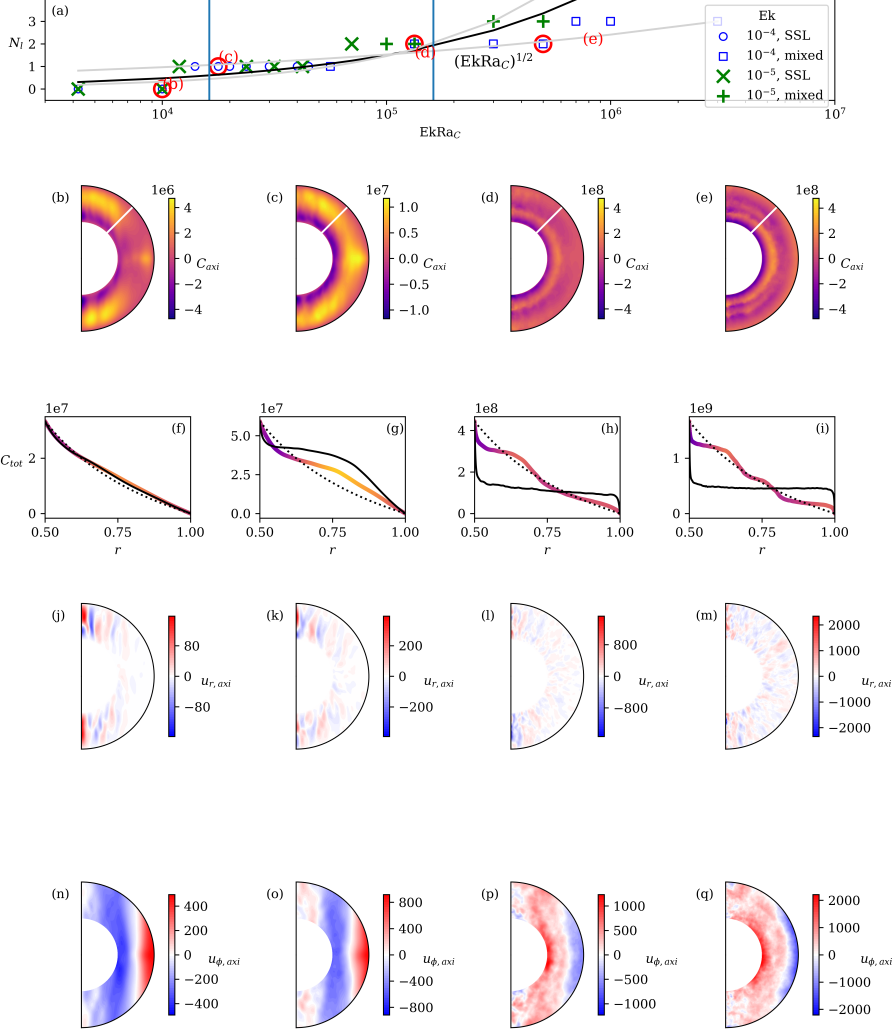


FIGURE 6. (a) Dependence of the number of layers  $N_l$  on  $\text{EkRa}_C$ , for simulations along transects  $R_\rho = 1.2$ , and  $\text{Ek} = 10^{-4}$  and  $10^{-5}$ , with  $\text{Pr} = 0.3$ ,  $\text{Sc} = 3$ , and  $\Delta R = 0.5$ . The black inclined lines show the relation  $N_l \propto \text{Ra}_C^{1/2}$ , while grey lines show lower and upper bounds on the scaling at powers 0.2 and 0.65. Squares/crosses represent simulations where the layers eventually decay to a state with a stably stratified layer overlaying a convective zone; circles/plusses represent cases where the final state is a well-mixed region over the majority of the domain. (b)–(q) show snapshots of the simulations marked in red in (a), with each column coming from a single simulation. (b)–(e) axisymmetric part of the perturbation composition field  $C_{\text{axi}}$ , for the simulations circled in red in (a). (f)–(i) radial profiles of the total axisymmetric composition field  $C_{\text{tot}} = C_{\text{axi}} + C_0(r)$  along the white lines in (b)–(e), coloured by the value of  $C_{\text{axi}}$ . Dotted black lines show the conductive profile  $C_0(r)$ , while the solid black line shows the final profile of  $C_{\text{tot}}(r)$  after the end of the layering phase. (j)–(m) axisymmetric part of the radial velocity field, (n)–(q) axisymmetric part of the azimuthal velocity field.

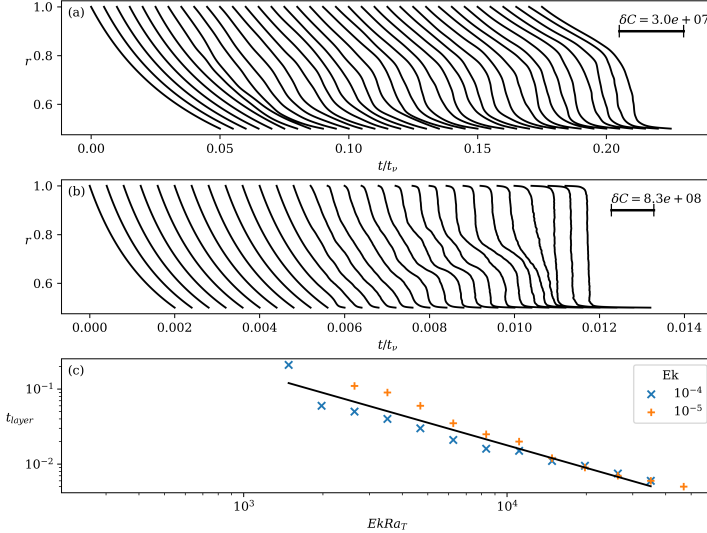


FIGURE 7. Profiles of  $C_{tot}(r)$  throughout the layered phase of two simulations, for (a)  $\text{Ra}_C = 1.77 \times 10^8$ , (b)  $\text{Ra}_C = 5 \times 10^9$ . Profiles are shown at a series of times, with a scale for the composition field shown in the top right. (c) Time spent in layered state  $t_{layer}$ , for simulations in the final convective zone regime.

We identify the height of the inner and outer stably stratified layers as

$$h_{in} = R_1 - R_i, \quad h_{SSL} = R_o - R_2. \quad (4.14)$$

Figure 8(a) shows how  $h$  varies as a function of the thermal forcing, for a range of simulations with  $10^{-6} \leq \text{Ek} \leq 10^{-4}$ . The majority of these simulations take  $R_\rho = 1.2$ ,  $\text{Pr} = 0.3$ , and  $\Delta R = 0.5$ , but these values were varied in a small number of simulations, while keeping  $L = 10$  constant. The data collapse onto a single curve  $h(R_B)$ , where we define the ‘rotational buoyancy number’

$$R_B = \text{Ek}^{3/2} \text{Ra}_T \text{Pr}^{-1}. \quad (4.15)$$

$R_B$  compares the competing effects of the unstable thermal stratification and the rotation, and is a form in which both length and thermal diffusivity are absent. The grey points show the value of  $h_{in}$ , which generally takes values significantly smaller than  $h_{SSL}$ , but follows a similar trend. Three regimes are clearly visible. For  $R_B < 35$ ,  $h_{SSL}/\Delta R$  is rather large, taking a value between 0.2–0.7, and scales rather weakly, with  $h_{SSL} \sim R_B^{-1/3}$ . For  $R_B > 35$ , there is a much stronger dependence, with  $h_{SSL} \sim R_B^{-3/2}$ . Above  $R_B \gtrsim 200$ , the trend shallows to  $h_{SSL} \sim R_B^{-1/3}$  once again.

These transitions can be explained in terms of the dependence of the Nusselt number on the SSL thickness. In Rayleigh–Bénard convection, the thermal boundary layer thickness is conventionally defined as  $\delta_T = H/(2\text{Nu})$ , where  $H$  is the layer thickness (e.g. Belmonte *et al.* 1994). The dependence of  $\text{Nu}$  on  $h_{SSL}$  is plotted in fig. 8(b), showing that a dependence  $\text{Nu} \sim h_{SSL}^{-1}$  until  $h_{SSL} \sim (\text{Ek}/\text{Pr})^{1/2}$  corresponds to the length above which the Coriolis force acts faster than thermal diffusion. Beneath this scale, the SSL acts as a thermal boundary layer. When the SSL is thicker, there is a shallower slope  $\overline{\text{Nu}} \sim h_{SSL}^{-1/2}$ . The transition between these two regimes is seen in fig. 8(a) at  $R_B \approx 200$ , where the trend in  $h$  sharply kinks in both  $\text{Ek} = 10^{-4}$  and  $\text{Ek} = 10^{-5}$  transects.

The transition at  $R_B \approx 35$  does not have a clear trace in 8(b), as the  $\overline{\text{Nu}}(h)$  dependence remains the same. On the other hand, fig. 8(c) shows a sharp jump in the value of  $\overline{\text{Nu}} - 1$

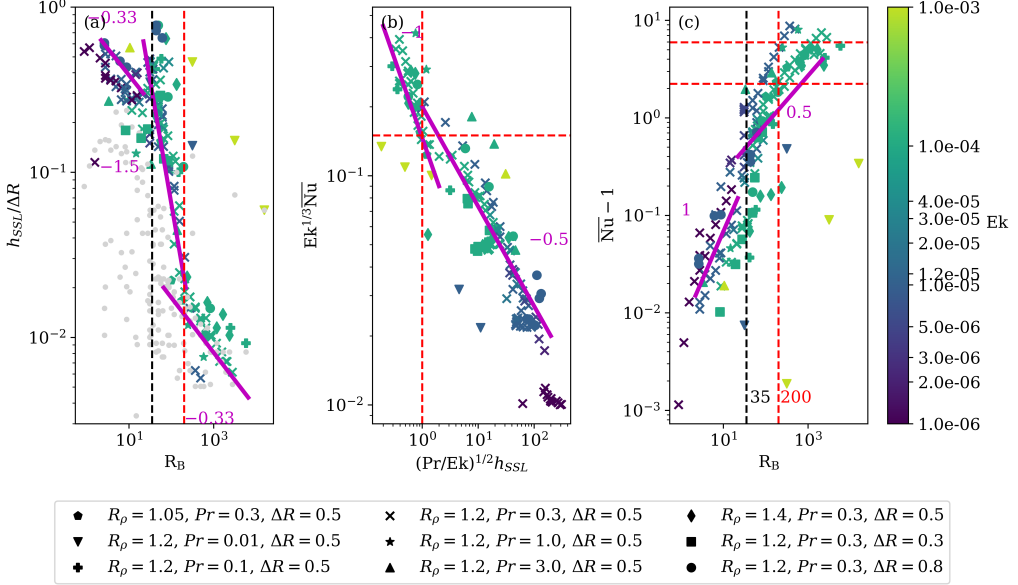


FIGURE 8. (a) Dependence of the height  $h_{SSL}$  of the outer stably stratified layer on  $R_B$ ; (b) variation of the Nusselt number at the outer boundary as a function of the rescaled SSL height  $(Pr/Ek)^{1/2}h_{SSL}$ ; (c) dependence of the time-averaged Nusselt number  $\bar{Nu}$  on  $R_B$ . Points are coloured by Ekman number  $Ek$ , with different values of  $R_\rho$ ,  $Pr$  and  $\Delta R$  represented by different symbols. Grey points in panel (a) show the width  $h_{in}$  of the inner boundary layer. The black dashed line in (a) and (c) marks a change in scaling for  $h$ , corresponding with a jump in  $\bar{Nu}$ ; red dashed lines in all panels show a transition as  $(Pr/Ek)^{1/2}h_{SSL}$  passed through unity.

at  $R_B = 35$ , as well as a change in scaling law, thus accounting for the transition seen in fig. 8(a). We shall see later that this jump is accounted for by a transition to turbulence.

### 4.3. Behaviour of the saturated semi-convection field

We now consider the dynamics beyond the layered phase, when the system has saturated to a statistically steady state. In § 4.2 we noted two regimes, with the post-layered state consisting of either a single convective region, or a convective zone overlain by a stably stratified layer with a mostly zonal flow. To understand the signature of these regimes on the global properties of the flow, we define Reynolds numbers based on the zonal-toroidal (ZT), and non-zonal-poloidal (NZP) components of the flow, which can be used as proxies for the amount of energy in zonal jets and in convective motions, respectively:

$$\text{Re}_{\text{jet}} = \frac{\sqrt{2\langle E_{ZT} \rangle_{\text{rms}} R_o}}{\nu}, \quad \text{Re}_{\text{conv}} = \frac{\sqrt{2\langle E_{NZP} \rangle_{\text{rms}} R_o}}{\nu}. \quad (4.16)$$

Figure 9(a)–(c) shows the dependence of  $\bar{Re}$ ,  $\bar{Re}_{\text{jet}}$  and  $\bar{Re}_{\text{conv}}$ , on  $\text{Ra}_C$  along the transect  $\text{Ra}_T = \text{Ra}_C/12$ , for  $Ek = 10^{-4}, 10^{-5}$  and  $10^{-6}$ . In general, as the forcing increases, the flow strength also increases. In § 4.2 we noted two visible transitions. These transitions are also visible in fig. 9, with a sudden jump in the value of  $\bar{Re}$  at  $R_B = 35$  (at  $Ro = 0.04$ ), and a saturation of the value of  $\bar{Re}_{\text{jet}}$  at  $R_B \approx 200$ . For the majority of simulations,  $\bar{Re}_{\text{jet}} \gg \bar{Re}_{\text{conv}}$ , with convective motions being more dominant only for  $R_B \gtrsim 200$ , where the outer stably stratified layer is thinner than  $(Ek/Pr)^{1/2}$ . Hereafter,

we will refer to the regime with  $R_B < 35$  as ‘‘jet-dominated’’, and above  $R_B > 35$  as ‘‘convection-dominated’’.

Figure 9(d) shows the mixing efficiency in the convective zone, calculated (following Vidal *et al.* 2018) as

$$\chi = 1 - \frac{\int_{R_1}^{R_2} \langle N^2 \rangle_{S(r)} dr}{\int_{R_1}^{R_2} \langle N_0^2 \rangle_{S(r)} dr}, \quad (4.17)$$

where  $\langle \cdot \rangle_{S(r)}$  is the mean over the spherical surface at radius  $r$ , and  $R_1$  and  $R_2$  are defined by (4.12)–(4.13). This quantifies how well-mixed the convective zone is, with  $\chi = 0$  when there is no departure from the background density profile, and  $\chi = 1$  when the convective zone is well-mixed to a constant density. Fig. 9(d) shows that, in the jet-dominated regime,  $\chi$  takes small values, but increases as a function of the forcing  $\text{Ra}_T$ . By contrast,  $\chi$  is large and relatively constant in the convective regime. This means that not only is the convective zone larger for values of  $R_B > 35$ , but the convection itself is also more efficient for mixing. In the jet-dominated regime,  $\chi$  is a function of  $\text{EkRa}_T$ ; however, the jet-convection transition still occurs at  $R_B$  for each transect.

The transition at  $R_B = 35$  is most obvious in the  $\text{Ek} = 10^{-4}$  transect, although is also present in the simulations with  $\text{Ek} = 10^{-5}$ . To explain this further, figure 10 shows snapshots of the velocity and temperature fields above and below the transition, for four simulations labelled by their position along the transect (cf. fig. 9). Below the transition (simulations 3 and 6), the dynamics is clearly dominated by strong columnar zonal jets visible in the  $u_\phi$  snapshots. The flow is fairly laminar, with relatively weak velocities, and some wave-like structures are visible along the top of the convective region. Above the transition (simulations 8 and 11), clear convective billows are seen in  $T$  and  $u_r$ , with significantly finer-scale structures than in the jet-dominated regime. Figure 10(o) shows the breakdown of the columnar structure in simulation 8 (just above the transition), with smaller-scale structures and marked asymmetry between the northern and southern hemispheres. In simulation 16, fig. 10(p) shows that  $u_\phi$  is very irregular, although traces still remain of the zonal jets, with generally prograde flow outside the tangent cylinder to the inner sphere, and retrograde flow inside.

The transition at  $R_B \approx 200$  has a much smaller visual trace on the flow, as seen by comparing simulations 11 and 16. The flow in 16 is smaller scale, with a narrower outer boundary layer, but the plots in fig. 10 appear qualitatively similar. This is because in this regime, the dynamics are dominated by behaviour in the large convective zone, with the SSL sufficiently small that a change in its depth has little trace on the global structure.

Figure 9 does not demonstrate a unified behaviour across different values of  $\text{Ek}$  and the whole range of  $R_B$ ; we shall discuss how data collapses on a single master curve later in § 5.

To quantify the turbulent transport in the flow, we consider the Nusselt and Sherwood numbers. We show the trend in the Nusselt and Sherwood numbers on the inner boundary as a function of  $\text{Ra}_C$  in fig. 11(a), for the same simulations as shown in fig. 9. At all points,  $\overline{\text{Sh}}$  is larger than  $\overline{\text{Nu}}$  (as the diffusive transport is naturally lower for the slower-diffusing scalar). For smaller values of  $\text{Ra}_C$ ,  $\overline{\text{Nu}}$  and  $\overline{\text{Sh}}$  are both close to unity, representing very low levels of convection. As  $\text{Ra}_C$  increases,  $\overline{\text{Nu}}$  and  $\overline{\text{Sh}}$  increase, scaling like  $\overline{\text{Nu}} - 1, \overline{\text{Sh}} - 1 \sim \text{Ra}_C^{5/4}$ . For comparison, Wood *et al.* (2013) found  $\overline{\text{Nu}} - 1 \sim \text{Ra}_C^{1/3}$  for non-rotating, layered semi-convection, while for rapidly rotating thermal convection, Gastine *et al.* (2016) found the upper limit on the power law to be  $\overline{\text{Nu}} - 1 \sim \text{Ra}_T^{3/2}$ . The 4/3 law that we obtain sits between these two limits.

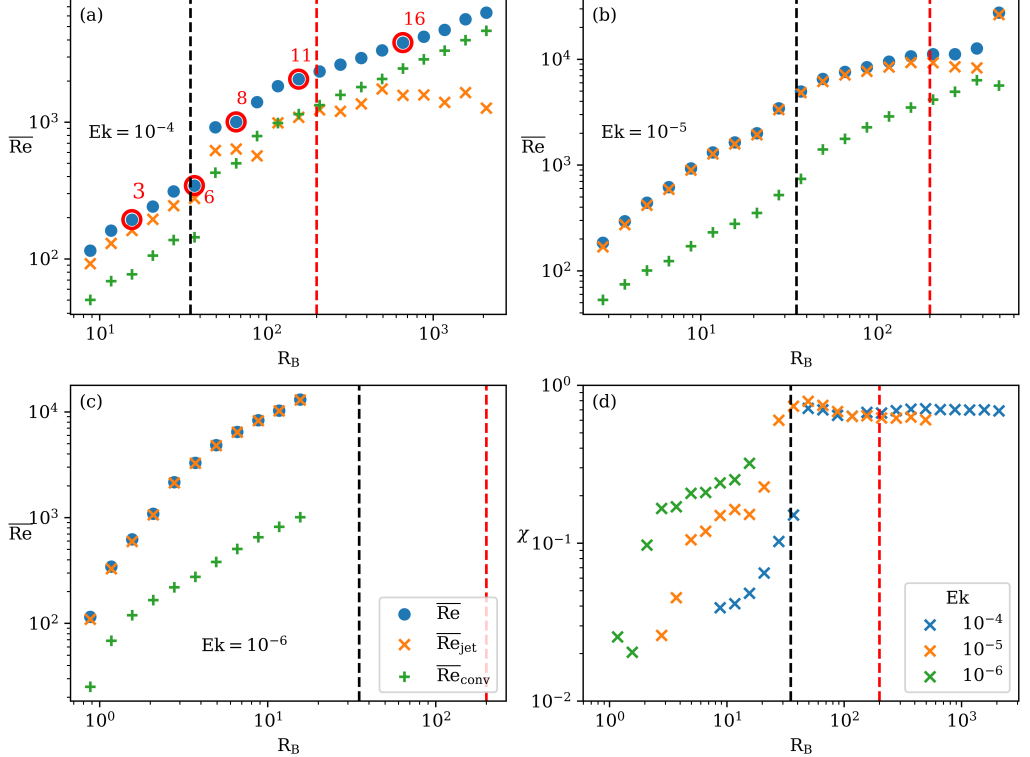


FIGURE 9. Time-averaged Reynolds number  $\overline{\text{Re}}$  plotted as a function of  $R_B$  for simulations with  $\text{Ra}_T = \text{Ra}_C/12$ ,  $\text{Pr} = 0.3$ ,  $\text{Sc} = 3$ ,  $\Delta R = 0.5$ , for (a)  $\text{Ek} = 10^{-4}$ , (b)  $10^{-5}$  and (c)  $10^{-6}$ . Blue points show the total Reynolds number, with orange and green showing the jet- and convection-based Reynolds numbers  $\overline{\text{Re}}_{\text{jet}}$  and  $\overline{\text{Re}}_{\text{conv}}$  respectively. Red circles mark simulations that are shown in detail in fig. 10. Red and black dashed lines mark the positions of the transitions seen in fig. 8 (d) Mixing efficiency  $\chi$  calculated in the long-term saturated state, plotted for three values of  $\text{Ek}$ .

The transition at  $R_B = 35$  is clearly visible in fig. 11(a), with a marked jump of a factor of ten in both  $\overline{\text{Nu}}$  and  $\overline{\text{Sh}}$ , and a change in the scaling law to  $\text{Ra}_C^{1/2}$ . In the fingering regime, Monville *et al.* (2019) found that  $\overline{\text{Nu}} - 1$  always remained small, meaning that the thermal transport was dominated by thermal diffusion, allowing small-scale fingering patterns to develop. By contrast, for larger values of  $\text{Ra}_C$ ,  $\overline{\text{Nu}} - 1$  achieves values larger than unity, due to the development of a two-layer system, with a vigorously convecting layer found beneath the SSL.

The trend in the convective power against  $R_B$  is shown in fig. 11(b). There is a remarkably clear scaling  $\overline{P} \sim \text{Ra}_C^2$ , but upon closer inspection, further trends can also be seen. In the jet-dominated regime for small values of  $\text{Ra}_C$ ,  $\overline{P}$  is very close to  $\overline{P}_T$ , with a smaller contribution from  $\overline{P}_C$ . However, above  $R_B > 35$ , where convection dominates,  $\overline{P}_C$  increases notably, resulting in smaller values of  $\overline{P}$ , with the scaling law  $\overline{P} \sim \text{Ra}_C^{3/2}$ . This matches with description of a convection-dominated flow, where both thermal and compositional fields are strongly disrupted by fluid motions, giving a value of  $\overline{P}_C$  that is close to  $-\overline{P}_T$ . Notably, the transition at  $R_B = 200$  is not visible in either the Nusselt/Sherwood numbers or the convective powers, similarly to what was observed in the flow snapshots.

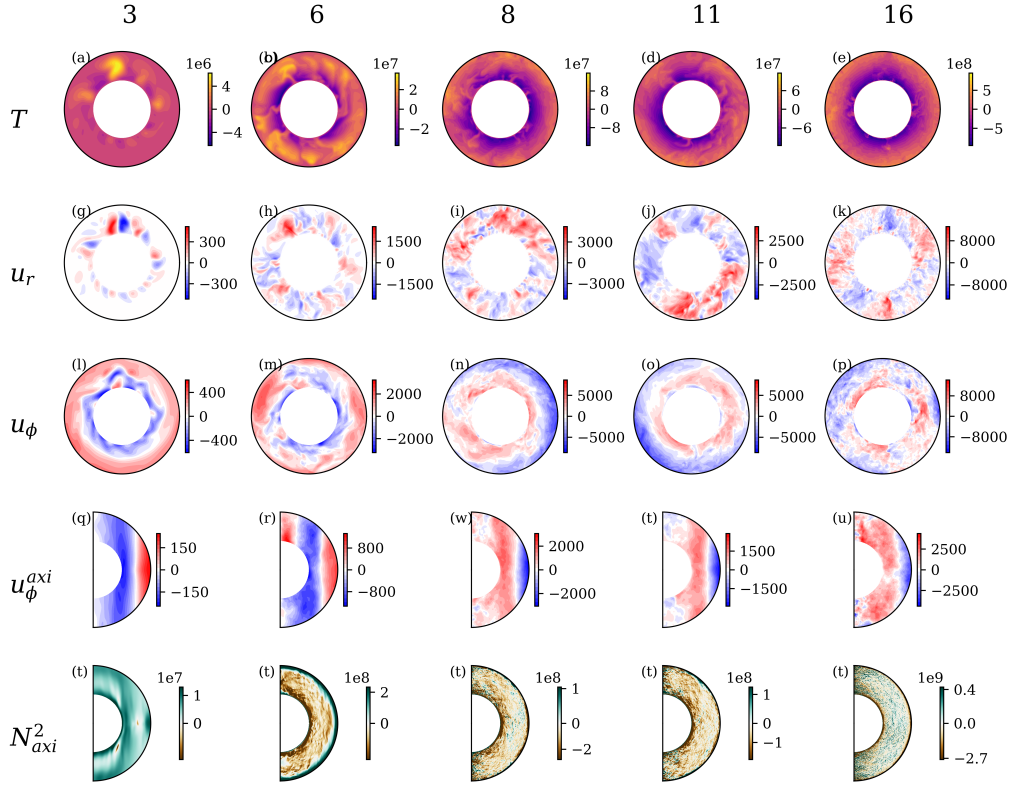


FIGURE 10. Snapshots of the five simulations marked by red circles in fig. 9. Each column shows results from a single simulation (labelled at the top). Each row shows, respectively, equatorial slices of the temperature perturbation  $T$ , radial velocity  $u_r$ , azimuthal velocity  $u_\phi$ , and meridional slices of the axisymmetric ( $m = 0$ ) part of the azimuthal velocity  $u_\phi^{axi}$  and axisymmetric squared Brunt-Väisälä frequency  $N_{axi}^2$ .

## 5. Dynamo generation by semi-convection

To investigate the possibility of dynamos driven by semi-convection, we now consider the full magneto-hydrodynamic Boussinesq equations, allowing  $\mathbf{b}$  to be non-zero in (2.2)–(2.5). We begin by discussing the favourable conditions for the dynamo to exist. The relative strength of magnetic advection to diffusion can be characterised by the magnetic Reynolds number

$$Rm = \frac{UL}{\eta} = \frac{\sqrt{2\langle E_u \rangle_{rms}} R_o}{\eta} = \text{PmRe}, \quad (5.1)$$

where  $U$  and  $L$  are characteristic velocity and length scales, and  $\text{Pm}$  is the magnetic Prandtl number (cf. table 1). When  $Rm \gg 1$ , advection dominates diffusion, and dynamo action is then possible. In planetary conditions  $\text{Pm} \ll 1$ , which imposes that  $\text{Re}$  must be large to produce a self-sustaining dynamo. Referring to fig. 9, this means that larger values of  $\text{Ra}_C$  are preferable.

Pružina *et al.* (2025) demonstrated that semi-convection can indeed lead to dynamo action at low magnetic Prandtl number. However, this initial study left many outstanding open questions. Notably, this paper focused on a single simulation, producing results relevant to a Jupiter-like configuration. A broader study is still required to understand

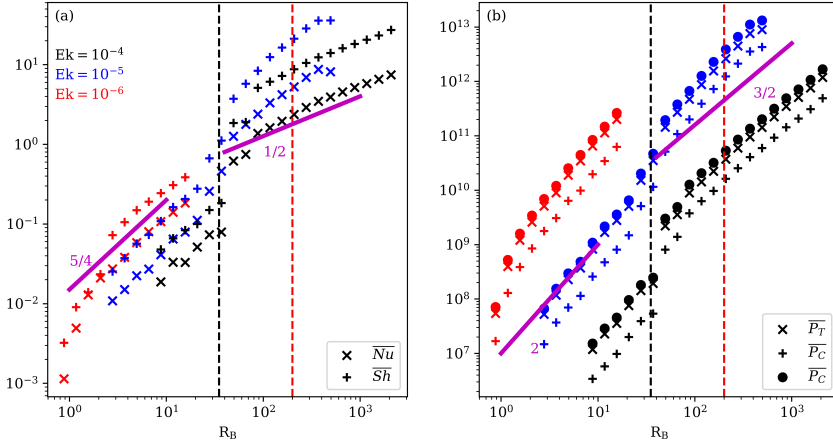


FIGURE 11. Quantities describing the strength of convection for simulations along the transect  $Rat = Ra_C/12$ : (a) Time-averaged Nusselt and Sherwood numbers on the inner boundary  $r = R_o = 0.5$ , with dashed lines showing the scaling  $|Ra_C|^{4/3}$  and solid lines  $|Ra_C|^{2/3}$  (b) Time-averaged Thermal, compositional and total convective power, with dashed lines showing  $|Ra_C|^{7/3}$  and the solid line  $|Ra_C|^{5/3}$ . Vertical dashed lines denote the positions of the transitions identified in fig. 8.

how the form of the magnetic field depends on the flow structure and dimensionless parameters. The behaviour near the onset is of particular interest.

The simulation discussed by Pružina *et al.* (2025) was in the jet-dominated regime, with the final state of the layered phase being an inner convective zone overlain by a stably stratified region. Fluid motions in this convective zone drive the dynamo to produce a magnetic field. Velocities are lower in the outer layer, although this alone does not necessarily prevent that region from also actively contributing to the dynamo.

To investigate the onset of the dynamo, we begin from the hydrodynamic simulations presented in § 4. Taking the saturated semi-convective state as an initial condition, we seed a random small-amplitude magnetic field perturbation and allow the system to evolve in time. After a short adjustment period, the magnetic field undergoes a linear growth/decay phase, with the magnetic energy  $E_m \sim \exp(\sigma t)$  for growth rate  $\sigma$ .

### 5.1. Dynamo action: onset and self-sustained regime

We begin by discussing the onset of dynamo action. The key parameter is the magnetic Reynolds number  $Rm$ ; for growth in the magnetic field,  $Rm$  must be sufficiently large. Figure 12(a) summarises a number of simulations for a range of  $Ek$ ,  $Ra_C$  and  $Pm$ , showing the value of  $Rm$  achieved, and whether or not a dynamo developed (diagnosed by growth/decay of the magnetic energy  $E_b$ ). It is clear that in general, larger values of  $Rm$  produce dynamo action; however, the onset appears to vary strongly with  $Ek$  and  $Pm$ . However, defining the magnetic Reynolds number based on the full domain neglects the fact that the convective flow is rather weak in the outer stably stratified layer. We instead define a convective magnetic Reynolds number, using the assumption that the convective part of the kinetic energy is contained entirely within the convective region.

$$Rm_{\text{conv}} = Pm \text{Re}_{\text{conv}} \left( \frac{R_o^3 - R_i^3}{R_2^3 - R_1^3} \right)^{1/2} \frac{R_2 - R_1}{R_o - R_i}. \quad (5.2)$$

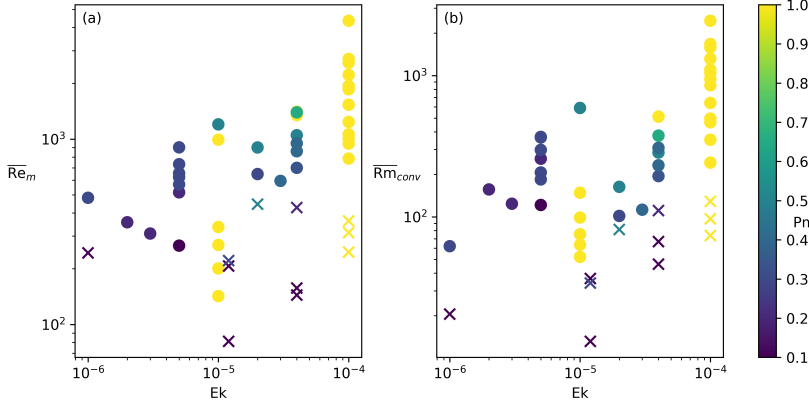


FIGURE 12. Summary of a large number of dynamo simulations, with (a)  $\overline{Rm}_m$  and (b)  $\overline{Rm}_{conv}$  plotted against  $Ek$ . Dots and crosses (coloured by  $Pm$ ) designate simulations with successful and unsuccessful dynamos, respectively. The dashed line in (b) is an estimate of the value  $\overline{Rm}_{conv}$  at the onset of dynamo.

where  $R_1$  and  $R_2$  are the inner and outer boundaries of the convective zone as defined by (4.12)–(4.13), and  $R_i$  and  $R_o$  are the inner and outer boundaries of the domain. Figure 12(b) shows the same data as panel (a), plotted with this new convective magnetic Reynolds number  $\overline{Rm}_{conv}$ . Here, the onset of dynamo action is much clearer, with the dashed black line marking an approximate transition between simulations with and without growth in magnetic energy. This confirms that the dynamo is only active in the convective zone, and not in the SSL.

Our simulations exist in both the weak and strong field regimes (defined as sub- and super-equipartition of magnetic over kinetic energies). Figure 13(a) shows the Rossby number  $Ro = EkRe$  against the rotational buoyancy number  $R_B$ , coloured by the ratio  $E_b/E_u$  (with hydrodynamic simulations shown as black crosses). The maximum value of  $E_b/E_u$  is 7.4, with all but 3 (resp. 20) simulations having  $E_b/E_u < 1$  (resp.  $E_b/E_u < 0.1$ ). For reference, we expect a value in the range  $1e-4 < E_b/E_u < 1$  for Jupiter (Pružina *et al.* 2025). In all cases, the Rossby number is not significantly affected by the magnetic field, with the MHD simulations broadly collapsing onto the same curve as the hydrodynamics simulations. Figure 13(b) shows  $Ro$  against the convective Rossby number  $Ro_C = Ek\sqrt{Ra_T/Pr}$ , coloured by  $h_{SSL}$ . While the data shows a wider spread at low  $Ro \lesssim 0.1$  compared to in fig. 13(a), the scaling at larger  $Ro$  is better. The low- $Ro$  regime characteristic of planets is associated with a wide SSL (and small  $R_B$  and  $Ro_C$ ), although we note that all simulations except three produced  $Ro < 1$ .

The majority of our simulations were carried out with  $\Delta R = 0.5$ ,  $Pr = 0.3$  and  $Sc = 3$ . While we conducted a small number of simulations with different values of  $\Delta R$  and  $Pr$ , the Lewis number  $L = Sc/Pr = 10$  was kept constant. While this value is not far from the relevant value for gaseous planets (e.g.  $L \approx 30$  in Jupiter Pružina *et al.* 2025), we cannot exclude a Lewis number dependence in the curves seen in fig. 13. This moderate value of  $L = 10$  also somewhat limits the region of parameters where semi-convection can be studied (see equation 3.10 and Fig 2); a larger value of  $L$  would increase the range of  $R_\rho$  allowed in simulations from  $1 \leq R_\rho \leq 3.25$  in this paper to  $1 \leq R_\rho \lesssim 10$  for Jupiter.

### 5.2. Dipolarity: effect of flow structure

The magnetic fields of giant planets such as Jupiter and Saturn, as well as the Earth, are strongly dipolar. As such, it is of considerable interest to identify trends in the

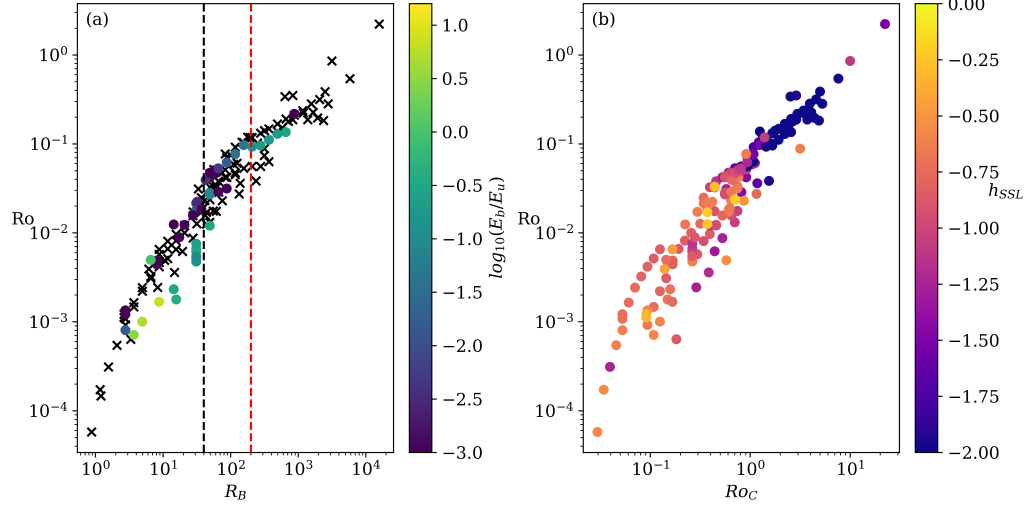


FIGURE 13. Rossby number  $\text{Ro} = \text{EkRe}$  plotted against (a) rotational buoyancy number  $R_B$ , coloured by the ratio of the magnetic to kinetic energies  $E_b/E_u$ , and (b) convective Rossby number  $\text{Ro}_C$ , coloured by the size of the stably stratified layer. In (a), black crosses mark hydrodynamic simulations, while black and red dashed lines show the position of the transitions at  $R_B = 35$  and  $200$ , respectively.

dipolarity of the magnetic field generated by the semi-convective dynamo. We quantify the dipolarity and axisymmetry using the dipole and axisymmetry fractions

$$f_{\text{dip}} = \sqrt{\frac{\sum_{m=0}^l (2 - \delta_{m0}) |\mathbf{b}(l=1, m, t)|^2}{\sum_{l,m \geq 0} (2 - \delta_{m0}) |\mathbf{b}(l, m, t)|^2}}, \quad (5.3)$$

$$f_{\text{axi}} = \sqrt{\frac{\sum_{m=0}^l (2 - \delta_{m0}) |\mathbf{b}(l, m=0, t)|^2}{\sum_{l,m \geq 0} (2 - \delta_{m0}) |\mathbf{b}(l, m, t)|^2}}, \quad (5.4)$$

where  $l$  and  $m$  are spherical harmonic degree and order,  $\mathbf{b}(l, m, t)$  is the  $(l, m)$  component of the magnetic field at the surface of the simulation  $r = R_o$ , and  $\delta_{ij}$  is the Kronecker delta function. Note that these definitions are not totally standardised: it is common to define  $f_{\text{dip}}$  using a spectrum truncated at the maximum  $l$  of the current models of the target planet's magnetic field.

Figure 14(a) shows how the dipole and axisymmetry fractions vary along a transect of dynamo simulations with  $\text{Ek} = 10^{-4}$ , as well as the ratio of the convective/jet Reynolds numbers. It appears that high values of  $f_{\text{dip}}$  and  $f_{\text{axi}}$  are associated with the jet-dominated regime. Figures 14(b)–(g) show snapshots of the magnetic field on the surface, and the axisymmetric part of the velocity, for two simulations, one in the jet-dominated regime, and one where convection dominates. In the first simulation, the surface magnetic field is clearly strongly dipolar, with a clear partition between the two hemispheres. The velocity field is dominated by strong jets, with  $u_r$  significantly smaller in magnitude than  $u_\phi$ . Figure 14(f) shows that this simulation is in the jet-dominated regime, with a wide outer stably stratified layer. This simulation closely resembles that considered by Pruzina *et al.* (2025). By contrast, in the second simulation, the magnetic field displays much more fine structure, with large contributions from higher- $l$  modes. The velocity jets are less columnar, and the radial velocity is of a similar magnitude to the azimuthal velocity, showing a much higher proportion of energy in convection

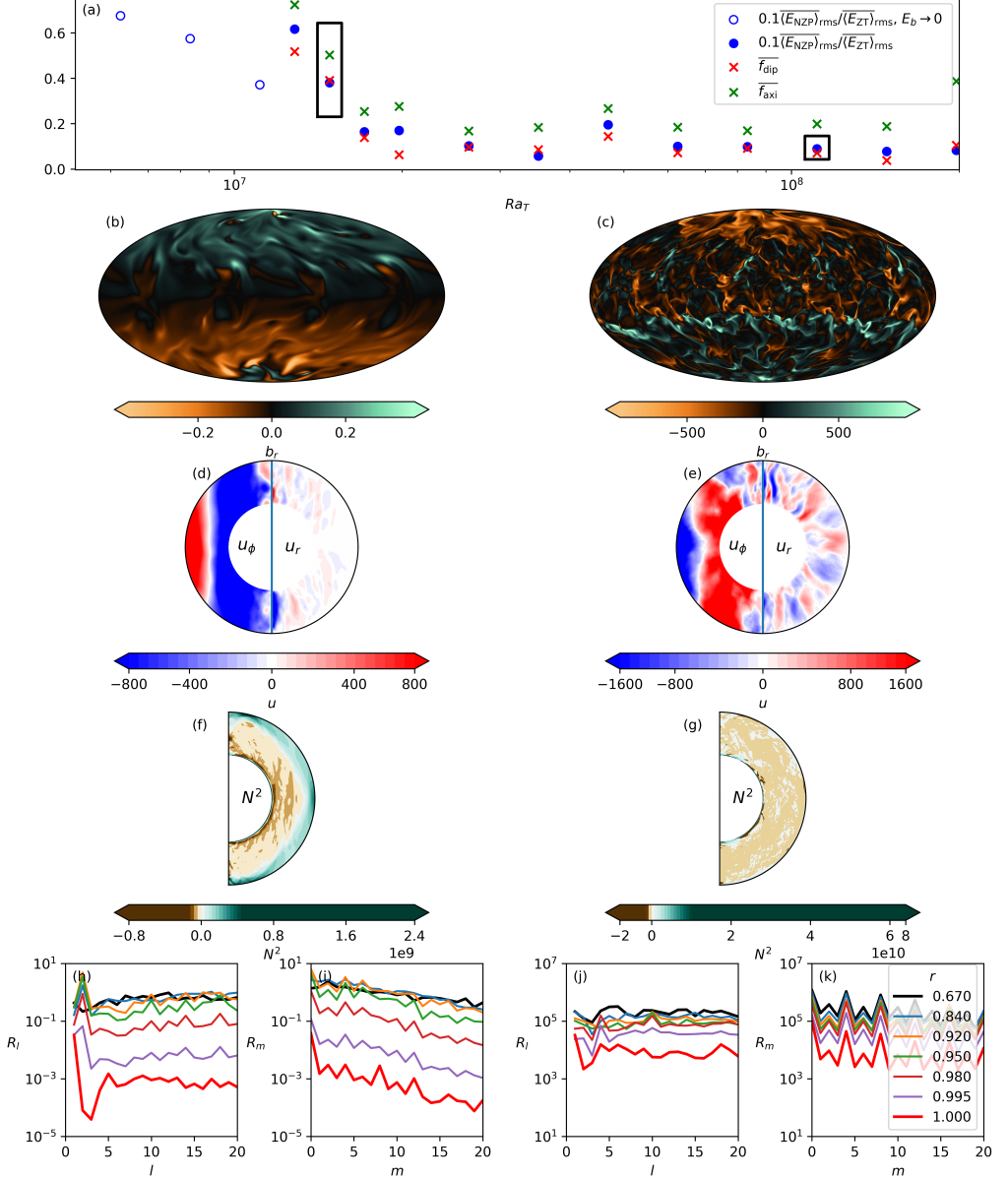


FIGURE 14. (a) Ratio  $\langle\bar{E}_{\text{NZP}}\rangle_{\text{ZT}}/\langle\bar{E}_{\text{jet}}\rangle_{\text{rms}}$ , and dipolar fraction  $\bar{f}_{\text{dip}}$ , along a transect of dynamo simulations with  $E_k = 10^{-4}$ . (b)–(g) Snapshots of the surface radial magnetic field  $b_r$ , axisymmetric part of the radial velocity field  $u_r$ , axisymmetric part of the azimuthal velocity  $u_\phi$  and squared Brunt-Väisälä frequency  $N^2$ , for the two simulations indicated in black boxes in (a). (h)–(k) Magnetic energy spectra in spherical harmonic degree  $l$  and order  $m$  for each simulation, at a range of radii from the deep interior to the surface.

compared to jets. Here, the convective zone takes up the entire domain, with much finer-scale density structures visible. Figure 14(h)–(k) show the magnetic energy spectra at a range of radii for each simulation; in both cases, the spectrum is rather flat in the interior, and does not change significantly in the convective region. Further out, in the SSL, the spectrum decays with radius, with the dipole ( $l = 1$ ) component decaying at the

slowest rate. In the jet-dominated regime, a wide SSL means that the field has decayed significantly and become strongly dipolar by the time it reaches the surface. By contrast, in the convection-dominated regime, the SSL is very thin, so the structure of the field at the surface is rather similar to that deep inside the shell. The effect of radius on the  $m$ -spectra is similar, with the  $m > 0$  modes decaying more rapidly as radius increases, resulting in an axisymmetric-dominated field at the surface.

### 5.2.1. A recipe for planetary magnetic fields?

It has been proposed (e.g. Stevenson 1982; Cao *et al.* 2011) that the magnetic field of Saturn is strongly axisymmetric and dipolar because of a stably stratified layer overlaying a convective zone where the field is generated. Simulations with an imposed SSL above the dynamo region confirm that this is possible (Yadav *et al.* 2022). Our simulations of semi-convection show that this structure can be generated spontaneously by semi-convection. With this in mind, we can identify the correct regions of parameter space to produce planet-like magnetic fields. A thick stably stratified layer is necessary to filter the field, so a small-as-possible value of  $R_B$  is preferable. However, velocities must also be large enough to generate a dynamo, so  $R_B$  must also be large enough to provide these turbulent flows. As such, a value  $R_B$  just greater than 35 should be ideal. Figure 8 showed that the scaling for  $h/\Delta R$  did not depend significantly on domain depth; therefore, a larger SSL can be obtained by simulating a thicker shell.

Based on these criteria, we present the results of a simulation for  $Ek = 10^{-5}$ ,  $Ra_C = 4.2 \times 10^9$ ,  $Ra_T = 3.5 \times 10^8$ ,  $Pr = 0.3$ ,  $Sc = 3$ ,  $Pm = 1$ , in a shell with  $\Delta R = 0.8$ . Note that these parameter values are rather moderate, so the simulation is not particularly computationally challenging, with a resolution of only  $(N_R, N_l, N_m) = (256, 200, 200)$  in the radial direction and spherical harmonic  $l$  and  $m$ . These values are chosen such that  $R_B = 36.8$ ; just to the right of the transition. Figure 15(a) shows the surface radial magnetic field for this simulation; the field is very strongly dipolar and axisymmetric. For comparison, fig. 15(b) shows the surface field if the fluid in the layer  $r_L \leq r \leq 1$  is insulating (calculated by setting the toroidal component of  $\mathbf{b}$  to zero, and the imposing poloidal component  $P(r) = P(r_L) \times (r/r_L)^{-l-1}$ , with  $r_L = 0.7$ ). This ‘truncated’ field is noticeably less dipolar and axisymmetric than the full field, and in general shows larger-scale structures.

Figure 15(c)–(e) show the axisymmetric  $m = 0$  part of the magnitude of the total and radial magnetic fields, squared Brunt–Väisälä frequency, and azimuthal and radial velocity fields. The black line shows the boundary between the convective zone and SSL. Inside the convective zone, the radial and azimuthal velocities are of a similar magnitude, and there is a strong magnetic field; in the SSL, the radial velocity becomes small, and the strength of the magnetic field drops (particularly the radial component).

Figure 15(f)–(g) shows spectra of the magnetic energy at a range of radii; deep in the interior, the  $l$  and  $m$  spectra are both rather flat, with no variation with depth. Closer to the surface, the power drops off sharply with radius, resulting in a surface field with very strongly dominant dipole ( $l = 1$ ) and axisymmetric ( $m = 0$ ) components, with  $\overline{f_{\text{dip}}} = 0.95$  and  $\overline{f_{\text{axi}}} = 0.99$ . Saturn’s magnetic field has dipole and axisymmetric fractions of  $f_{\text{dip}} \approx 0.99$  and  $f_{\text{axi}} \approx 0.985$  (Cao *et al.* 2020), so our simulation compares rather favourably. The blue dashed lines in figs. 15(f)–(g) show the surface power spectra of the truncated magnetic field (with an insulator for  $r_L \leq r \leq 1$ ). Compared to the full spectra, these profiles show a slower decay at low values of  $l$  and  $m$ , with values of  $\overline{f_{\text{dip}}} = 0.87$  and  $\overline{f_{\text{axi}}} = 0.92$  — markedly smaller than for the full magnetic field. This greater dominance of  $l = 1$  and  $m = 0$  of the full field demonstrates that the flow in the

SSL actively filters the magnetic field, rather than simply acting as an insulating layer where the field decays (as discussed by, e.g. Stevenson 1982).

## 6. Conclusions

In recent years, significant attention has been focused on double-diffusive convection in astrophysical bodies, with new structure models of gas giants proposing that large regions of planetary cores may be unstable to semiconvection. With this in mind, we have presented a detailed numerical study of semi-convection in rotating spherical shells, in the low- $\text{Pr}$  regime appropriate for these astrophysical applications.

### 6.1. Results summary

The linear semi-convection instability closely follows two limits. When the gradient of the stabilising scalar is relatively weak, the onset of instability is at the critical value  $\text{Ra}_{T,\text{crit}}$  for rotating thermal convection. When the stratification is strong, instability occurs at the onset of semi-convection found in a local stability analysis of a non-rotating fluid. Between these two limits, there is a rather smooth transition, particularly for larger values of  $\text{Ek}$ . For faster rotation rates, the ‘tongue’ found by Monville *et al.* (2019) for the fingering regime exists, slightly extending the critical Rayleigh number beneath the rotating convection limit. However, this effect is much less pronounced than in the fingering case, with no change at higher spherical harmonic orders.

Looking past the linear instability, we performed numerical simulations using the XSHELLS spherical harmonic solver. For weak thermal forcing, the linear semi-convection instability grows, eventually saturating in a weakly non-linear state. When the forcing is stronger, however, complex non-linear behaviour is seen. After a linear growth phase, well-mixed layers of relatively constant density form, separated by interfaces with large density gradients. Over time, these layers gradually merge together, leaving a single well-mixed region in the domain. The formation of layers follows the widely accepted  $\gamma$ -instability, which states that layers will develop if the ratio of the thermal to compositional fluxes decreases as a function of the ratio of their gradients (Radko 2003). However, in our simulations, the depth of the layers is rather large compared to the domain size, meaning that for weaker forcing, there is not enough space for layers to form. The majority of our simulations were performed along a transect with  $R_\rho = 1.2$ , meaning that we changed the total strength of the stratification by varying  $\text{Ra}_C$  and  $\text{Ra}_T$ , while keeping the distance from onset relatively constant.

Over time, the layers merge (following the B-merger pattern described by Radko (2007)), leaving a wide convective region in the middle of the domain. For strong forcing, the convective region occupies almost the entire domain, with only narrow stably stratified boundary layers at the top and bottom. However, for weaker forcing, a wide stably stratified layer sits above the convective region. The dimensionless height  $h_{SSL}/\Delta R$  of this layer depends on the rotational buoyancy number  $R_B \equiv \text{Ek}^{3/2}\text{Ra}_T\text{Pr}^{-1}$  (in which the length and thermal diffusivity vanish). There are three scaling regimes: when the forcing is small, the SSL takes up a significant portion of the domain, with a rather weak dependence on the forcing. Above the transition to turbulence,  $h_{SSL}$  decreases dramatically with  $\text{Ra}_T$ . Finally, once  $h_{SSL} \sim (\text{Ek}/\text{Pr})^{1/2}$ , the behaviour matches that of a thermal boundary layer.

In general, the flow strength (measured by the Reynolds number) increases with forcing (measured by  $R_B$ ). When the SSL is large, the flow is dominated by zonal jets in the SSL, with convective motions confined to the inner convective region. As the SSL reduces

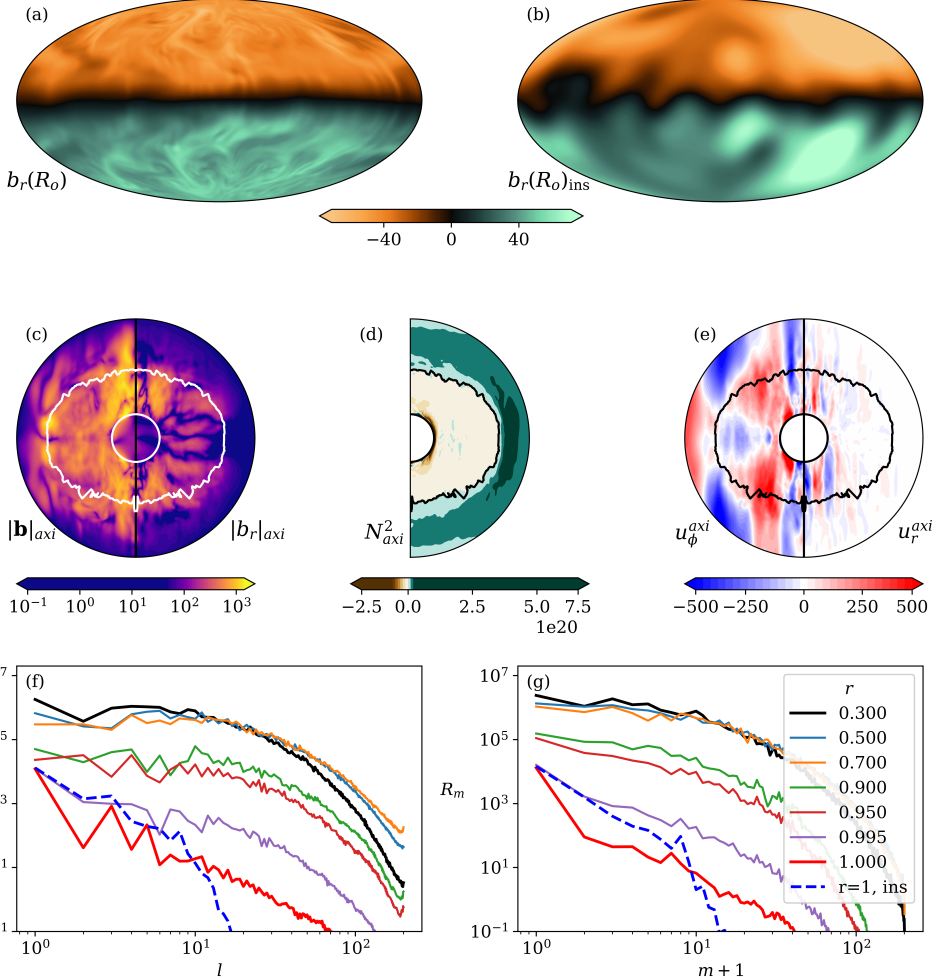


FIGURE 15. Results from a simulation with  $\text{Ek} = 10^{-5}$ ,  $\text{Ra}_C = 4.2 \times 10^9$ ,  $\text{Ra}_T = 3.5 \times 10^8$ ,  $\text{Pr} = 0.3$ ,  $\text{Sc} = 3$ ,  $\text{Pm} = 1$ ,  $\Delta R = 0.8$ , showing (a) surface magnetic field  $b_r$ , (b) surface field when the fluid in  $0.7 \leq r \leq 1$  is insulating, and axisymmetric parts of the (c) magnitude of the magnetic field  $|\mathbf{b}|$ , and radial magnetic field  $|b_r|$  (d) square of the Brunt-Väisälä frequency  $N^2$ , (e) radial and azimuthal velocity, (f)  $l$ -spectrum and (g)  $m$ -spectrum of the magnetic energy at a range of radii, with the surface spectra for the insulating outer layer case shown as blue dashed lines. The boundary between convective and stably stratified regions, and the inner boundary of the fluid domain, are marked on the polar plots in white/black.

in size, the relative strength of zonal jets reduces, with convective motions becoming dominant at the  $h_{SSL} \sim (Ek/Pr)^{1/2}$  transition. All our simulations collapse onto a single master curve for Rossby number in terms of  $R_B$ , with the small-Ro regime applicable to gaseous planets associated with small  $R_B$  and a large SSL.

Magnetohydrodynamic simulations reveal that the flow regime (jet or convection-dominated) has a significant effect on the magnetic field. In the jet-dominated regime, the dynamo exists in the deep convection region, with the magnetic field smoothed out within the SSL, resulting in a weak surface field dominated by the dipolar, axisymmetric components. This smoothing in the SSL is more efficient than a simple insulating layer, resulting in stronger dipole and axisymmetry fractions, which implies that strong zonal flows in the SSL actively filter the field to produce a strong  $l = 1, m = 0$  dominance. In convection-dominated simulations, the full multipolar field survives to the surface, with a relatively flat spectrum altered only by a very thin stably stratified thermal boundary layer.

Since observed planetary fields are generally strongly dipolar and (especially for Saturn) axisymmetric, we identify a criterion to simulate a relatively realistic planetary dynamo. To maximise the size of the SSL to filter the magnetic field, the forcing must be as weak as possible. However, the flow must also be sufficiently strong to drive a dynamo. A choice of parameters just above the transition to turbulence balances these two criteria well. A numerical simulation for  $R_B = 20.2$  in a wide shell produces a SSL extending throughout more than half of the shell thickness, with a very strong surface dipole  $f_{dip} = 0.95$  and axisymmetry  $f_{axi} = 0.99$ , confirming our prediction for the favourable parameter range, and providing good evidence that a dynamo of this form may contribute to planetary magnetic fields. This mechanism of a deep SSL filtering the magnetic field to result in the observed dipolar/axisymmetric field has been theorised for several decades (e.g. Stevenson 1982), and in recent years simulations with an imposed SSL above a convective zone have produced results that compare very favourably to the magnetic field of Saturn (Yadav *et al.* 2022). Our contribution is to demonstrate that both the convective layer generating the field, and the SSL to filter it can be the result of the natural evolution of the fluid in a wide region with boundary conditions suggesting semi-convection. The dipole and axisymmetry fractions of the magnetic field in our simulation compare favourably to those observed in Saturn (Cao *et al.* 2020). We do not consider other metrics, such as flow structure or dipole tilt, as we do not claim to present a planetary model in this study, but rather to demonstrate the possible applications of a dynamo generated by semi-convection layering.

## 6.2. Perspectives

In this work, we have made a number of assumptions that should be discussed. Firstly, we considered the Boussinesq equations, neglecting differences in density except in conjunction with gravitational acceleration. For planetary applications, the validity of this approximation hinges on density variations being fairly small across the semi-convection region. In reality, the density is expected to vary rather significantly, especially for larger semi-convection regions as proposed for Saturn. However, for an initial survey, and from hydrodynamic interest, the Boussinesq approximation reveals a lot about the dynamics of semi-convection. While being simpler computationally than alternatives, it allows the investigation of more extreme parameter values.

We also assumed that both gravitational acceleration and electrical conductivity (influencing the magnetic diffusivity) were constant with depth. In planetary semi-convection, neither of these assumptions is strictly true, and allowing for a variable conductivity would be an interesting and useful extension to this work. Similarly, allowing

for the density ratio  $R_p$  to vary in space would provide a more realistic planetary simulation.

Several planetary models explain the decrease with radius of helium concentration as ‘helium rain’ (e.g. Howard *et al.* 2024). With a saturation concentration  $C_s(T)$  defined as a function of temperature, any composition exceeding this value  $C > C_s$  is considered to condense, leading to a ‘moist convection’ model. Leconte *et al.* (2017) show that, in the limit of fast condensation, semi-convection is completely suppressed, causing no fluid motion. They suggest that gas giants are indeed in this limit, which would imply that in the helium rain layer, heat transfer occurs only through radiation. However, if condensation is not totally instantaneous, semi-convection may not be fully inhibited, and the inclusion of a semi-convection region can explain all the observed gravitational and atmospheric constraints for Jupiter and Saturn (Leconte & Chabrier 2012). A further extension could be made to this work by the inclusion of condensation, as a third process competing against semi-convection and rotation.

*Acknowledgements:* The authors thank F. Debras for discussions about the existence of semi-convection layers in gaseous planets, and their potential to drive a dynamo. We also thank J. Vidal for assistance with the SINGE code.

*Funding:* Work funded by the ERC under the European Union’s Horizon 2020 research and innovation program via the THEIA project (grant agreement no. 847433), by the European High-Performance Computing Joint Undertaking (JU) under grant agreement 101093038 (CHEESE-2P), and by the NumPEX PEPR program ANR-22-EXNU-0006. Computations on the GRICAD infrastructure (<https://gricad.univ-grenoble-alpes.fr>), and HPC resources (Jean Zay V100 and H100) of IDRIS under allocation AD010413621 and A0160407382 attributed by GENCI (Grand Equipement National de Calcul Intensif).

*Author contribution statement:* PP produced the simulations, the figures, and the draft. DC came up with the initial research concept, and obtained the funding. NS modified the numerical code and helped with computations. DC and NS obtained computation hours from GENCI. All authors discussed each step of the work and the results; all edited the final manuscript.

*Declaration of interests:* The authors report no conflicts of interest.

## REFERENCES

BELMONTE, A., TILGNER, A. & LIBCHABER, A. 1994 Temperature and velocity boundary layers in turbulent convection. *Physical Review E* **50** (1), 269.

BREUER, M., MANGLIK, A., WICHT, J., TRÜMPER, T., HARDER, H. & HANSEN, U. 2010 Thermochemically driven convection in a rotating spherical shell. *Geophysical Journal International* **183** (1), 150–162.

CAO, H., DOUGHERTY, M. K., HUNT, G. J., PROVAN, G., COWLEY, S. W., BUNCE, E. J., KELLOCK, S. & STEVENSON, D. J. 2020 The landscape of saturn’s internal magnetic field from the cassini grand finale. *Icarus* **344**, 113541.

CAO, H., RUSSELL, C. T., CHRISTENSEN, U. R., DOUGHERTY, M. K. & BURTON, M. E. 2011 Saturn’s very axisymmetric magnetic field: No detectable secular variation or tilt. *Earth and Planetary Science Letters* **304** (1-2), 22–28.

CHRISTENSEN, U. R. & AUBERT, J. 2006 Scaling properties of convection-driven dynamos in rotating spherical shells and application to planetary magnetic fields. *Geophysical Journal International* **166** (1), 97–114.

DEBRAS, F. & CHABRIER, G. 2019 New models of jupiter in the context of juno and galileo. *The Astrophysical Journal* **872** (1), 100.

DORMY, E., SOWARD, A., JONES, C., JAULT, D. & CARDIN, P. 2004 The onset of thermal convection in rotating spherical shells. *Journal of Fluid Mechanics* **501**, 43–70.

FRENCH, M., BECKER, A., LORENZEN, W., NETTELmann, N., BETHKENHAGEN, M., WICHT, J. & REDMER, R. 2012 Ab initio simulations for material properties along the jupiter adiabat. *The Astrophysical Journal Supplement Series* **202** (1), 5.

FUENTES, J. 2025 3d simulations of semiconvection in spheres: Turbulent mixing and layer formation. *The Astrophysical Journal* **982** (1), 44.

FUENTES, J., HINDMAN, B. W., FRASER, A. E. & ANDERS, E. H. 2024 Evolution of semiconvective staircases in rotating flows: Consequences for fuzzy cores in giant planets. *The Astrophysical Journal Letters* **975** (1), L1.

GASTINE, T., WICHT, J. & AUBERT, J. 2016 Scaling regimes in spherical shell rotating convection. *Journal of Fluid Mechanics* **808**, 690–732.

GRAY, M., GUERVILLY, C. & SARSON, G. 2025 Influence of rotation on fingering convection in planetary cores. *arXiv preprint arXiv:2511.11442*.

HOWARD, S., MÜLLER, S. & HELLED, R. 2024 Evolution of jupiter and saturn with helium rain. *Astronomy & Astrophysics* **689**, A15.

JONES, C. 2014 A dynamo model of jupiter's magnetic field. *Icarus* **241**, 148–159.

LECONTE, J. & CHABRIER, G. 2012 A new vision of giant planet interiors: Impact of double diffusive convection. *Astronomy & Astrophysics* **540**, A20.

LECONTE, J. & CHABRIER, G. 2013 Layered convection as the origin of saturn's luminosity anomaly. *Nature Geoscience* **6** (5), 347–350.

LECONTE, J., SELSIS, F., HERANT, F. & GUILLOT, T. 2017 Condensation-inhibited convection in hydrogen-rich atmospheres-stability against double-diffusive processes and thermal profiles for jupiter, saturn, uranus, and neptune. *Astronomy & Astrophysics* **598**, A98.

LEDOUX, P. 1947 Stellar models with convection and with discontinuity of the mean molecular weight. *Astrophysical Journal* **105**.

MANKOVICH, C. R. & FULLER, J. 2021 A diffuse core in saturn revealed by ring seismology. *Nature Astronomy* **5** (11), 1103–1109.

MATHER, J. F. & SIMITEV, R. D. 2021 Regimes of thermo-compositional convection and related dynamos in rotating spherical shells. *Geophysical & Astrophysical Fluid Dynamics* **115** (1), 61–84.

MERRYFIELD, W. J. 1995 Hydrodynamics of semiconvection. *Astrophysical Journal, Part 1 (ISSN 0004-637X)*, vol. 444, no. 1, p. 318-337 **444**, 318–337.

MIROUH, G. M., GARAUD, P., STELLMACH, S., TRAXLER, A. L. & WOOD, T. S. 2012 A new model for mixing by double-diffusive convection (semi-convection). i. the conditions for layer formation. *The Astrophysical Journal* **750** (1), 61.

MOLL, R. & GARAUD, P. 2016 The effect of rotation on oscillatory double-diffusive convection (semiconvection). *The Astrophysical Journal* **834** (1), 44.

MONVILLE, R., VIDAL, J., CÉBRON, D. & SCHAEFFER, N. 2019 Rotating double-diffusive convection in stably stratified planetary cores. *Geophysical Journal International* **219** (Supplement\_1), S195–S218.

MOVSHOVITZ, N., FORTNEY, J. J., MANKOVICH, C., THORNGREN, D. & HELLED, R. 2020 Saturn's probable interior: an exploration of saturn's potential interior density structures. *The Astrophysical Journal* **891** (2), 109.

MÜLLER, S., HELLED, R. & CUMMING, A. 2020 The challenge of forming a fuzzy core in jupiter. *Astronomy & Astrophysics* **638**, A121.

PRUŽINA, P. 2025 A one-dimensional model of staircase formation in diffusive convection. *Journal of Fluid Mechanics* **1008**, A29.

PRUŽINA, P., CÉBRON, D. & SCHAEFFER, N. 2025 Planetary dynamos driven by semi-convection in stratified layers. *Astronomy & Astrophysics* **703**, A135.

RADKO, T. 2003 A mechanism for layer formation in a double-diffusive fluid. *Journal of Fluid Mechanics* **497**, 365–380.

RADKO, T. 2007 Mechanics of merging events for a series of layers in a stratified turbulent fluid. *Journal of Fluid Mechanics* **577**, 251–273.

ROSENBLUM, E., GARAUD, P., TRAXLER, A. & STELLMACH, S. 2011 Turbulent mixing and layer formation in double-diffusive convection: Three-dimensional numerical simulations and theory. *The Astrophysical Journal* **731** (1), 66.

SCHAEFFER, N. 2013 Efficient spherical harmonic transforms aimed at pseudospectral numerical simulations. *Geochemistry, Geophysics, Geosystems* **14** (3), 751–758.

SCHWARZSCHILD, M. 1958 *Structure and Evolution of Stars. Princeton Legacy Library* . Princeton University Press.

SCHWARZSCHILD, M. & HÄRM, R. 1958 Evolution of very massive stars. *Astrophysical Journal*, vol. 128, p. 348 **128**, 348.

STEVENSON, D. 1982 Reducing the non-axisymmetry of a planetary dynamo and an application to saturn. *Geophysical & Astrophysical Fluid Dynamics* **21** (1-2), 113–127.

STEVENSON, D. J., BODENHEIMER, P., LISSAUER, J. J. & D'ANGELO, G. 2022 Mixing of condensable constituents with h-he during the formation and evolution of jupiter. *The Planetary Science Journal* **3** (4), 74.

TIMMERMANS, M.-L., TOOLE, J., PROSHUTINSKY, A., KRISHFIELD, R. & PLUEDDEMANN, A. 2008 Eddies in the canada basin, arctic ocean, observed from ice-tethered profilers. *Journal of Physical Oceanography* **38** (1), 133–145.

TURNER, J. S. 1979 *Buoyancy effects in fluids*. Cambridge university press.

VAZAN, A., HELLED, R., PODOLAK, M. & KOVETZ, A. 2016 The evolution and internal structure of jupiter and saturn with compositional gradients. *The Astrophysical Journal* **829** (2), 118.

VIDAL, J., CÉBRON, D., SCHAEFFER, N. & HOLLERBACH, R. 2018 Magnetic fields driven by tidal mixing in radiative stars. *Monthly Notices of the Royal Astronomical Society* **475** (4), 4579–4594.

VIDAL, J. & SCHAEFFER, N. 2015 Quasi-geostrophic modes in the earth's fluid core with an outer stably stratified layer. *Geophysical Journal International* **202** (3), 2182–2193.

WOOD, T. S., GARAUD, P. & STELLMACH, S. 2013 A new model for mixing by double-diffusive convection (semi-convection). ii. the transport of heat and composition through layers. *The Astrophysical Journal* **768** (2), 157.

YADAV, R. K., CAO, H. & BLOXHAM, J. 2022 A global simulation of the dynamo, zonal jets, and vortices on saturn. *The Astrophysical Journal* **940** (2), 185.